*Small Structures*

small structures
Open Access
www.small-structures.com

RESEARCH ARTICLE OPEN ACCESS

# Organometallic Solution and Surface Routes to Highly Dispersed Carbon Nanotube-Based Fe–N–C Electrocatalysts

Jörg J. Schneider[1] | Chandrajeet Mohapatra[1] | Johannes M. Emmert[1] | Isabel M. Teichert[1] | Jörg Engstler[1] | Anna A. Makarova[2] | Kirill V. Yusenko[3] | Maciej Oskar Liedke[4] | Ahmed G. Attallah[4] | Maik Butterling[4] | Andreas Wagner[4] | Di Wang[5] | Christian Kübel[5] | Arpad Rostas[6] | Emre Erdem[7] | Martin Panthöfer[8] | Angela Möller[8]

[1]Eduard-Zintl-Institute, Inorganic and Mesoscopic Chemistry, TU Darmstadt, Darmstadt, Germany | [2]Helmholtz-Zentrum Berlin für Materialien und Energie, BESSY II, Berlin, Germany | [3]Federal Institute for Materials Research and Testing (BAM), Berlin, Germany | [4]Institute of Radiation Physics, Helmholtz-Zentrum Dresden-Rossendorf, Dresden, Germany | [5]Institute of Nanotechnology (INT) and Karlsruhe Nano Micro Facility (KNMFi), Karlsruhe Institute of Technology, Karlsruhe, Germany | [6]National Institute for Research and Development of Isotopic and Molecular Technologies, Cluj-Napoca, Romania | [7]Faculty of Engineering and Natural Sciences and Center of Excellence for Functional Surfaces and Interfaces for Nano-Diagnostics (EFSUN), Sabanci University, Istanbul, Turkey | [8]Department of Chemistry, Johannes Gutenberg-University, Mainz, Germany

**Correspondence:** Jörg J. Schneider (joerg.schneider@tu-darmstadt.de)

**Received:** 14 May 2026 | **Revised:** 8 September 2026 | **Accepted:** 6 October 2026

**Keywords:** atomic layer deposition | iron atoms | metal-atom synthesis | oxygen reduction reaction | single atom catalysts

## ABSTRACT

Herein, we demonstrate for the first time how reactive organometallics can be utilized as synthetic synthons in solution and on surfaces under chimie douce conditions to access Fe–N–C catalysts with single iron sites. Fe atoms are incorporated into nitrogen-binding sites of vertically aligned nitrogen-doped carbon nanotubes (VA-NCNTs), employing a solvated metal-atom dispersion SMAD approach and the organometallic precursor ($\eta^6$-toluene)Fe($\eta^2$-ethene)$_2$ derived therefrom to synthesize a Fe–N–C material **A** active as ORR catalyst. In an alternative synthetic approach, we introduce ALD utilizing bis($\eta^5$-ethyl-cyclopentadienyl)Fe and $H_2$ as precursors to access an Fe–N–C catalyst material **B**. HAADF–STEM, Mössbauer, magnetic measurements, XPS, and EPR confirm that iron is well dispersed in both Fe–N–C materials. This can be attributed to a controlled low iron loading avoiding formation of iron metal clusters and inorganic phases revealing the utmost importance of a controlled loading process. The porous VA-NCNT host material enhances active site accessibility and prevents catalyst aggregation as studied by PALS. Electronically, the embedded iron centers are long-range magnetically coupled across the CNT network. Overall, the study demonstrates a new alternative synthetic approach to widely used pyrolysis methods for catalytically active Fe–N–C SACs under so far unprecedented mild conditions.

## 1 | Introduction

Iron-based catalysts embedded in a nitrogen/carbon-based environment catalogized as Fe–N–C catalysts have prominently entered the field of nonprecious metal-containing single-atom catalysts (SACs) over the last decade. Their catalytic activity is high, and iron is envisaged as a surrogate for precious metals especially in the oxygen reduction reaction (ORR) [1–5]. Such Fe–N–C SACs promise metal-atom-economic reactions when they are highly dispersed and stabilized in a suitable chemical surrounding.

K. V. Yusenko's Current adress is the Institute of Geology, Mineralogy and Geophysics, Ruhr-University Bochum, Bochum, Germany.

This is an open access article under the terms of the Creative Commons Attribution License, which permits use, distribution and reproduction in any medium, provided the original work is properly cited.

© 2026 The Author(s). *Small Structures* published by Wiley-VCH GmbH.

Despite tremendous research efforts and successes in finding new active Fe–N–C SAC materials, most often triggered by their enhanced functionality in ORR, the utmost synthetic approaches to these materials rely solely on thermal transformations. These are dominated by pyrolytic routes of various N-containing organic compounds and metal salts or solid-state materials, e.g., metal–organic framework structures (e.g., ZIF8 [5, 6]) for achieving high dispersion of the iron metal sites. Common to these approaches is the incorporation of SAC centers in carbon matrices to achieve high catalyst performance. A severe drawback, however, are the high temperatures necessary for the Fe–N–C generation in all of these approaches [7]. Agglomeration and nucleation of single atoms to form α- or γ-iron nanoparticles or clusters, iron nitride, iron carbide, and iron chalcogenides (O,S), as well as hydroxides, are thus inherent to these synthetic routes [7, 8]. Most often, severe cleaning protocols to remove such unwanted byproducts are necessary [9, 10]. These species generated during thermal pathways may interfere and even in some cases show catalytic activities for ORR itself, making the identification of Fe–N–C active sites cumbersome [10–17]. For those, it is mostly accepted that iron in a fourfold coordination geometry around nitrogen embedded in a carbonaceous framework is the dominant active site in Fe–N–C catalysts [18–26]; however, $FeN_3$, $FeN_4$, and $FeN_5$ sites [27] have been discussed too [28, 29]. However, an exact determination and control of the N-doping sites in carbon nanotubes (CNTs) still remains elusive, which includes the exact coordination geometry of the embedded Fe centers in N-CNTs bearing catalytic activity.

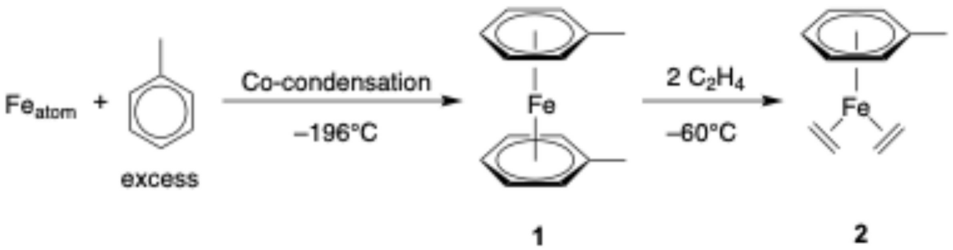
When a Fe–N–C center is introduced into a curved extended carbon framework as in CNTs, the electronic structure, geometry, and Fe *d*-valence situation undergo drastic changes in comparison to the planar structure and hence influence the catalytic activity of the material [18, 30–33]. Theoretically, it could be shown that an "outer" carbon environment of about eight C atoms in the second coordination sphere around the central iron in such an $FeN_4$ coordination is sufficient for the ORR activity [34]. Theory further reveals that an embedment of $FeN_4$ centers into an even larger 6 × 6 matrix of carbon ring fragments is even adequate for understanding spectroscopic properties in such Fe–N–C materials [18]. Another report has shown that 12 carbon atoms in a porphyrinic coordination environment ($\kappa^2$-pyrrolic coordination) in the second coordination sphere of iron have revealed—based on XANES K edge studies supported by DFT-theory—ORR-active Fe–N–C catalyst materials [4]. However, the situation of what can be expected from an even more extended and electronically coupled larger $\pi$ system as in graphene or CNTs on the electronic situation of precisely embedded Fe–N–C centers is still underexplored.

When approaching low-temperature processes to introduce iron atoms into carbon matrices under ambient conditions, the high free energy of solution-derived zerovalent free naked metal atoms always leads to strong metal-atom agglomeration already at low temperatures [35–38]. However, if the temperature is low enough to increase the nucleation barrier between isolated iron atoms, there is the possibility to atomically disperse these atoms even in solution, offering a new approach for Fe–N–C formation. The metal atoms can then eventually be stabilized in a suitable coordination environment of N-donor atoms incorporated into a carbon host. Nitrogen-doped CNTs represent such an environment and have been under investigation for their applicability as N-doped carbon support for SACs [39, 40].

We herein introduce a route to Fe–NC SACs in solution employing highly labile organometallic compounds containing zerovalent iron. The starting point is the synthesis of the dark green-brown bis($\eta^6$-toluene)Fe compound **1** which is stable only up to about −60 °C in excess toluene if no suitable reaction partners are offered (Scheme 1). For such a solution, the term solvated metal-atom dispersion (SMAD) has been coined [41]. If a frozen solution of iron atoms and toluene is reacted with an excess of ethene gas at $T < -120$ °C and warmed up to −30 °C, a deep yellow-orange solution of the reactive but more stable ($\eta^6$-toluene)Fe($\eta^2$-ethene)$_2$ **2** is formed (Scheme 1) [28]. In that way, the originally high reactivity of **1** can be tamed in a higher temperature range up to 0 °C. Solutions of **1** and **2** may thus be excellent precursors for the incorporation of single iron atoms into N-functionalized CNTs.

In an alternative synthetic approach, we study the incorporation of single iron atoms still under relatively mild conditions of 250 °C using an atomic layer deposition (ALD)-type approach. Herein, iron atoms are generated from the organometallic precursor molecule 1,1′-bis(ethyl)ferrocene and $H_2$ (Scheme 2).

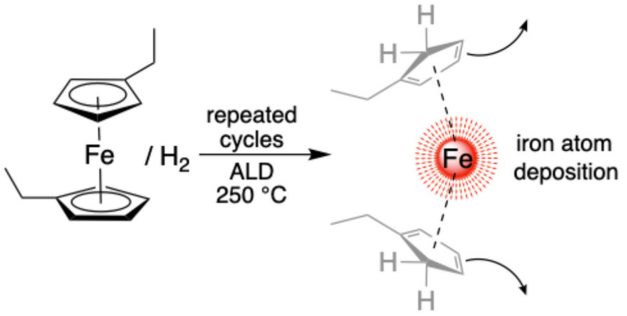
This modified ALD technique with its recurring deposition/reaction cycles is intended to generate iron atoms on the curved surface of vertically aligned nitrogen-doped carbon nanotubes (VA-NCNTs), where they will react with surface-embedded N-donor atoms. We use single-atom integration cycles for the incorporation into the N-doped CNT framework. It is noteworthy that both the solution-based method and the solid-phase ALD-type approach may offer a delicate synthetic balance of delivering single metal centers toward N-coordination sites by controlling the deposition stoichiometry. In the solution-phase route, this is done by adjusting the precursor concentration; in the ALD-type approach, it is achieved by adjusting the number of repeating deposition/reaction cycles of the organometallic precursor and reactant hydrogen.




**SCHEME 1** | Metal-atom route to the bis(arene)iron sandwich **1** and the half-sandwich iron complex **2**. **1** is stable up to −60 °C and **2** up to 0 °C under high dilution in toluene.



26884062, 2026, 11, Downloaded from https://onlinelibrary.wiley.com/doi/10.1002/sstr.70646 by Karlsruher Institut Fur Technologie, Wiley Online Library on [19/11/2026]. See the Terms and Conditions (https://onlinelibrary.wiley.com/terms-and-conditions) on Wiley Online Library for rules of use; OA articles are governed by the applicable Creative Commons License




**SCHEME 2** | Generation of single iron centers by a concerted ALD-type hydrogenation/decomposition process starting from 1,1′-bis(ethyl)-ferrocene at 250 °C. Hydrogenation of the $EtCp^-$ ligands leads to release of the cyclopentadiene moieties and extrusion of reactive iron atoms.

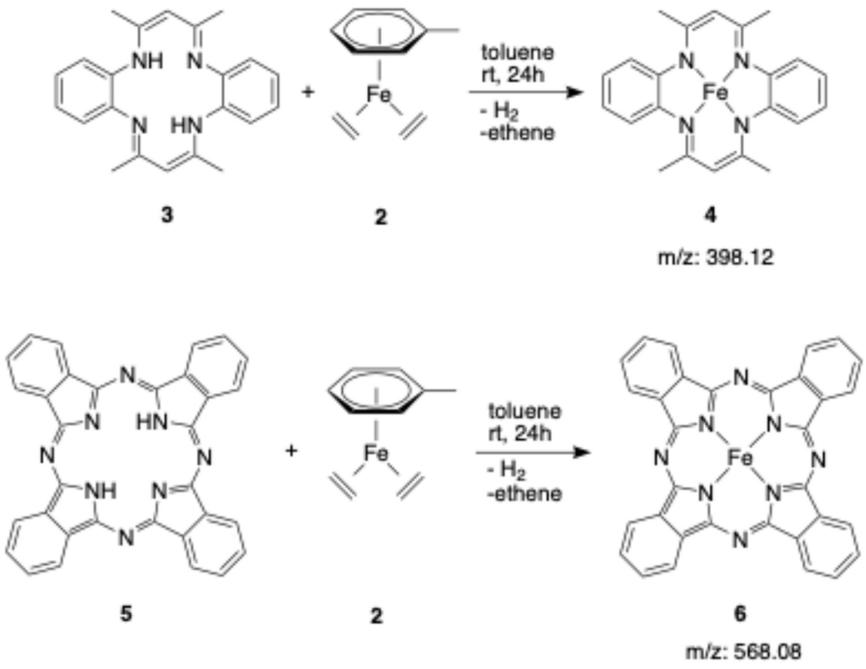
## 2 | Results and Discussion

### 2.1 | Synthesis

First, we introduce N-centers into multiwalled CNTs using pyridine as a carbon and nitrogen single-source precursor. We grow vertically aligned nitrogen-doped CNT architectures (VA-NCNT) under a high aspect ratio l:r (about 20 µm high, ca. 10-nm diameter; l:r = 2000) on a flat silicon wafer by a catalytically enhanced thermally driven chemical vapor deposition (CVD) process (see the Section 4 and Figures S1 and S2). Compared to randomly oriented NCNTs on a flat surface, which are highly entangled, VA-NCNTs allow better accessibility of individual NCNT surface sites due to the controlled arrangement of individual CNTs in this architecture. The introduction of nitrogen centers in the CNT surface creates donor coordination sites, which provide strong σ-anchoring capabilities for the tethering of iron atoms. These prevent further unwanted aggregation of single iron atoms, e.g., into iron dimers, trimers, or higher nucleated iron clusters or even fine particles if the iron atom concentration of precursor **2** in solution is sufficiently low. N-heteroatom introduction in CNTs goes along with a change in hybridization $sp^2$ versus $sp^3$ and a further increase in bending of the NCNTs' carbon framework, causing an enhancement in chemical reactivity. Active sites in such N-doped CNTs for ORR are the positively polarized $C^{\delta+}$ atoms next to the pyridinic $N^{\delta-}$ centers [42–45]. A first indication that organometallic precursor **2** is indeed reactive toward an *N*-heterocyclic ligand environment under ambient conditions stems from the reaction of **2** with isolated phthalocyanine and porphyrin ligand molecules **3** and **5** as molecular probes under ambient conditions (Scheme 3). Formation of the corresponding iron macrocyles **4** (*m*/*e* 398.1192; calc. **4**: $C_{22}H_{22}N_4Fe = m/e$ 398.1188) and **6** (*m*/*e* 586.0844; calc. **6**: $C_{32}H_{16}N_8Fe = m/e$ 568.0842) can be identified by HR-MS as the sole identifiable products of this insertion reaction.

Following this, a $2 \times 2\,cm^2$ dense array of VA-NCNTs (ca. 20 µm in height, ca. 1 mg) grown by CVD on a silicon wafer is reacted with a solution of organometallic compound **2** in toluene containing 29.5 µmol/mL iron between −30° and room temperature over the course of 24 h (Scheme 4). The deep yellow solution of **2** moderately lightens, indicating the reaction of **2** with N-VACNTs (Figure S3). After workup, the resulting black powder was thermally treated at 300 °C for 30 min under vacuum to remove remaining adsorbed free toluene from the VA-NCNT surface.

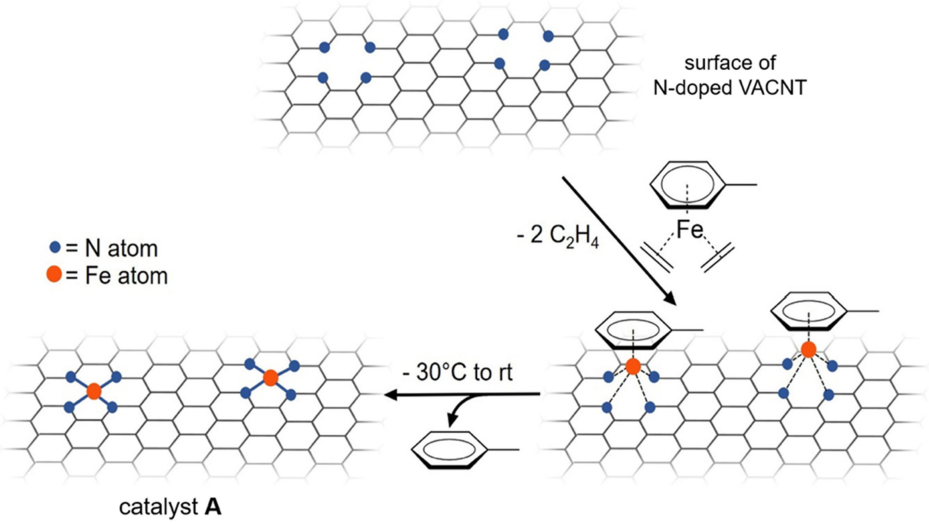
To study the direct surface approach to generate iron atoms, bis($\eta^5$-ethyl-cyclopentadienyl)Fe **7** was deposited consecutively with $H_2$ at 250 °C onto VA-NCNTs employing ALD. The optimized ALD process cycle employs 50 cycles of deposition (Scheme 5), followed by a postannealing step at 500 °C/30 min under vacuum. This ensures that the VA-NCNT host is free of remaining organic residues from the ALD process, as it is proven by TG-MS (Figure S4).




**SCHEME 3** | Reaction of *N*-heterocycles **3** and **5** with **2** to form the iron heterocycles **4** and **6** under ambient conditions.



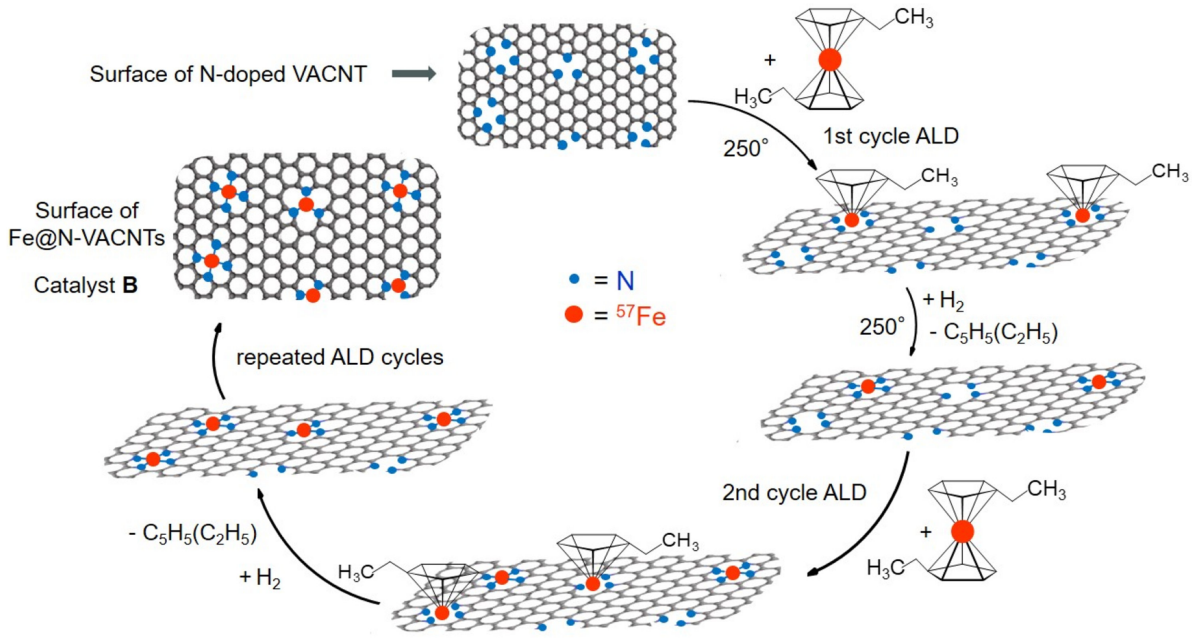
26884062, 2026, 11, Downloaded from https://onlinelibrary.wiley.com/doi/10.1002/sstr.70646 by Karlsruher Institut Fur Technologie, Wiley Online Library on [19/11/2026]. See the Terms and Conditions (https://onlinelibrary.wiley.com/terms-and-conditions) on Wiley Online Library for rules of use; OA articles are governed by the applicable Creative Commons License




**SCHEME 4** | Schematic representation showing the solution deposition process under low temperature to ambient conditions. Intermediate formation of [($\eta^6$-toluene)Fe] half-sandwich fragments and subsequent ethene extrusion leads to catalyst **A**. The graphene-type cutout shown represents an idealized model structure of a CNT surface; the bending according to the diameter of the CNTs is neglected here for clarity.

In both synthetic approaches leading to catalyst materials **A** and **B**, the initial coordination of half sandwich type fragments [($\eta^6$-toluene)Fe] (generated from precursor **2**) or [($\eta^5$-ethyl-Cp)Fe] (generated from precursor **7**) to the N-doped curved graphitic surface of VA-NCNTs can be assumed [46–50].

The Fe content in **A** as determined by inductively coupled plasma optical emission spectroscopy (ICP-OES) is 0.8 wt%, respectively, 0.5 wt% for **B**, assuring a low iron incorporation for both materials **A** and **B**. This outcome further excludes the presence of metal cluster/particle formation within the detection of the method. The additional challenges with high metal loadings in solution-based synthesis processes for SACs have been addressed [51]. It should be noted that similar results allowing a high iron dispersion can be obtained when instead of **2**, the organometallic sandwich compound **1** is reacted with VA-NCNTs at −60 °C; however, the effectively usable temperature window for this reaction is very narrow with respect to exclusion of unwanted metal deposition and aggregation, which already starts below −50 °C, making the approach using **2** more feasible. In the following studies, all samples are handled under ambient conditions (air, temperature) throughout.




**SCHEME 5** | Scheme showing the ALD type deposition process for the formation of catalyst material **B** using ferrocene derivative **7** and $H_2$ as reducing agent. The graphene type cut out shown represents an idealized model structure of a CNT surface; thus, the bending according to the diameter of the CNTs is neglected here for clarity.



26884062, 2026, 11, Downloaded from https://onlinelibrary.wiley.com/doi/10.1002/sstr.70646 by Karlsruher Institut Fur Technologie, Wiley Online Library on [19/11/2026]. See the Terms and Conditions (https://onlinelibrary.wiley.com/terms-and-conditions) on Wiley Online Library for rules of use; OA articles are governed by the applicable Creative Commons License

## 2.2 | Electron Microscopy

Catalyst materials **A** and **B** have been further characterized by SEM, HRTEM, and STEM–HAADF. All microscopy studies confirm the absence of any unwanted higher nuclearity side products after iron deposition (Figures 1 and S5).

HAADF–STEM imaging is highly sensitive to changes in the atomic number (~$Z^{1.7}$) in addition to the sample thickness, giving stronger scattering events for iron than for nitrogen and carbon. A STEM–HAADF image of **A** thus gives a first meaningful indication for the presence of well-dispersed isolated iron centers in the N-CNT host matrix (Figure 2). It employs a high-angle annular dark-field detector for incoherent imaging down to atomic resolution. The isolated iron centers show up as bright spots scattered over the NCNT surface. Additional evidence for the nitrogen embedment of iron atoms stems from the EELS analysis, which delivers characteristic N and Fe edge spectra, albeit with low iron in corporation (Figure S6). Nevertheless, it should be mentioned that visualizing an isolated Fe–N–C entity has not yet been achieved [17]. In our case, this is due to the embedment of the iron atoms in a multifaceted carbon framework, which is especially challenging due to the bent and bamboo-shaped tubular structure of the N-CNTs, which renders the identification of such individual centers highly difficult.

In the **Raman** spectrum of **A** and **B**, signals at 1338 $cm^{-1}$ (D1) and at 1577 $cm^{-1}$ (D2) for the VA-NCNTs matrix with an $I_D/I_G$ ratio of 1.68 (A) and 1.71 (B) are indicative of the defective-rich morphology of the Fe@N-CNTs compared to the bare VA-NCNTs ($I_D/I_G = 1.34$) (Figures S7 and S8).

## 2.3 | XPS

High-resolution XPS spectroscopy provides further information on the elemental composition and chemical states of Fe–N–C centers in **A** and **B** (Figure 3 and Table 1). It reveals six different components in N 1s spectra for both catalysts **A** and **B**: pyridinic-N; graphitic-N; pyrrolic-N; N atoms connected to Fe, characteristic of Fe–NC centers [27]; N–O or N–H coordination; and molecular $N_2$ [52]. The latter signal is further corroborated in NEXAFS N K-edge spectra in the photon energy range between 400.5 and 402 eV and discussed below separately (see Figure 4c). It is notable that the concentration of Fe–N–C centers is higher by about 30% in **A** as compared to **B**. This might be attributable to the higher iron content, as it is determined by OCP-OES. The solution synthetic route (see Scheme 4) obviously allows for a higher reaction yield of active Fe–N–C centers on the surface of VA-NCNTs than the surface deposition route (see Scheme 5). The C 1*s* spectra of **A** and **B** are characterized by an asymmetrical line-shape of the dominating peak centered at 284.5 eV, together with a shake-up satellite peak at around 291 eV. This signature is characteristic of the $sp^2$-hybridized graphitic carbon network. The shoulder at the higher binding energy side indicates the contribution of a minor amount of $sp^3$-hybridized carbon, presumably with C–N and C–O functionalities (Figure S9).

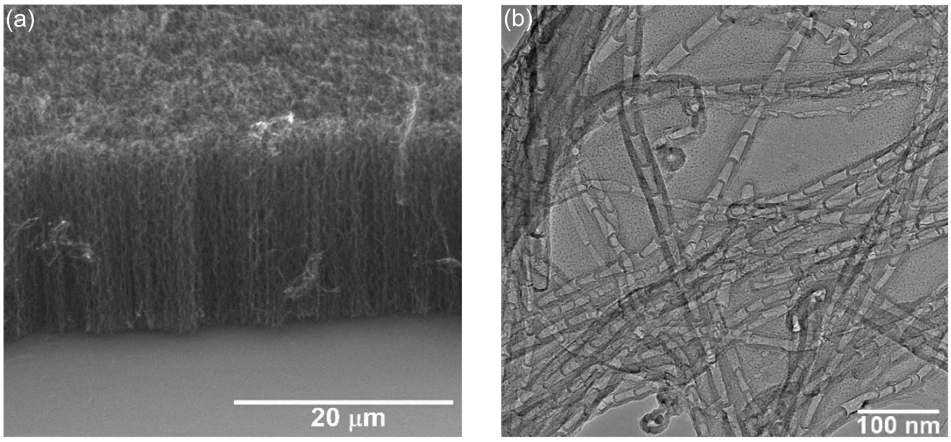



**FIGURE 1** | (a) SEM of multiwalled bamboo-type shaped VA-NCNTs as obtained by CVD synthesis using pyridine as carbon/nitrogen source. (b) TEM of isolated N-CNTs after reaction with the iron compound **2** (catalyst **A**). For HRTEM of catalyst **B** (ALD derived), see Figure S5. The isolated Fe@NCNTs in (b) are unhinged from the Fe@VA-NCNT array by sonification in ethanol. No visible presence of clusters or fine particles is found in the separated bamboo-type Fe@NCNTs of **A** (b).

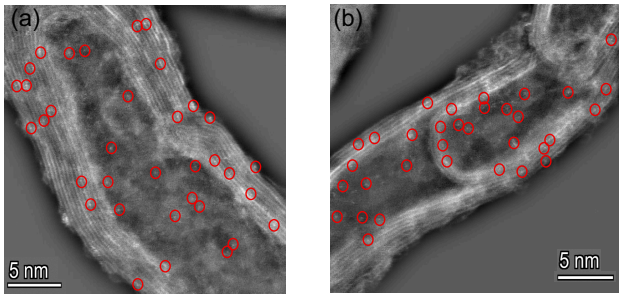



**FIGURE 2** | Aberration-corrected HAADF–STEM images of catalysts **A** and **B**. (a) Catalyst **A**, obtained from complex **2**, showing atomically dispersed iron within the CNT wall structure; (b) catalyst **B**, obtained from complex **7** under ALD-type conditions, likewise exhibiting isolated iron atoms. The images were processed by a high pass filter employing Velox software for better contrasting (Thermo Fisher Scientific).



26884062, 2026, 11, Downloaded from https://onlinelibrary.wiley.com/doi/10.1002/sstr.70646 by Karlsruher Institut Fur Technologie, Wiley Online Library on [19/11/2026]. See the Terms and Conditions (https://onlinelibrary.wiley.com/terms-and-conditions) on Wiley Online Library for rules of use; OA articles are governed by the applicable Creative Commons License

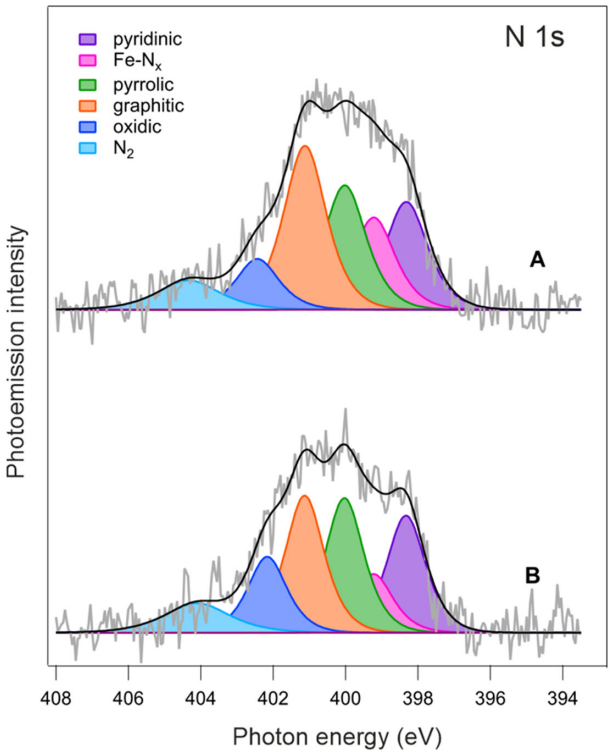



**FIGURE 3** | High-resolution N 1s core-level spectra (hν = 830 eV) of catalyst **A** and **B** derived from solution synthesis route (A) and from surface chemistry route by ALD type reaction (B) together with the results of fitting analysis. Background is subtracted for clarity.

**TABLE 1** | Chemical composition and percentage of nitrogen-containing species in catalyst materials **A** and **B** as determined by XPS.

| Chemical assignment | Binding energy, eV | | Relative amount, at% | |
|---|---|---|---|---|
| | A | B | A | B |
| Pyridinic | 398.3 | 398.3 | 18.6 | 20.5 |
| $N_x$–Fe | 399.2 | 399.2 | 15.9 | 10.3 |
| Pyrrolic | 400.0 | 400.0 | 21.4 | 23.5 |
| Graphitic | 401.1 | 401.1 | 28.2 | 24.0 |
| Oxidic | 402.5 | 402.2 | 8.7 | 13.3 |
| Molecular $N_2$ | 404.5 | 404.1 | 7.3 | 8.6 |

## 2.4 | XANES

The NEXAFS spectra of catalysts **A** and **B** at the C K-edge (Figure 4b) are dominated by two main features at ca. 285.4 eV and ca. 291.5 eV related to electron transitions from the 1 s level to the graphitic-like π* and σ* states, respectively [53]. The presence of these peaks confirms the well-ordered structure of the graphitic networks of the VACNT architecture. Features arising at around 288 eV are related to low amounts of oxidized species, most probably carboxyl groups, which are together with some defects in the carbon framework (see Raman spectra) typically located at edges and defect sites of the NCNTs. The intensity of this signal may increase with prolonged storage of the sample under ambient conditions. NEXAFS spectroscopy at the N K-edge of **A** and **B** samples reveals several π*-resonances in the range from 397 to 404 eV and broad σ*-resonance placed at 407.5 eV (Figure 4a). Distinct features at around 398.5 eV correspond to pyridinic nitrogen and at 399.8 eV either to pyrrolic or Fe–NC [54]. A feature with characteristic intensity at higher energies is related to the entrapping of molecular $N_2$. This signal overlaps with the one typical for graphitic-like nitrogen [52, 55–57]. Vibrational splitting of the enlarged peak allows an assignment to molecular nitrogen (see the inset of Figure 4c) corresponding to entrapped $N_2$ molecules inside the entangled nanotube arrangement. It originates from the VA-NCNT synthesis process, which uses pyridine as a precursor [55, 56].

Intriguing are the NEXAFS Fe $L_{2,3}$-edge spectra in the BE region 705–725 eV, which give information on the valence and spin state of iron in **A** and **B**, although the spectral intensity is low due to the minute loading of iron (around 0.5%). For **A** and **B**, signals at 708 and 710 eV for the $L_3$ edge spectra (Fe transitions from $2p_{3/2}$ to 3d) and between 719 and 725 eV in the $L_2$ edge region (Fe transitions from $2p_{1/2}$ to 3d) are observed. The habitus of the spectral shape of **A** and **B** differs from the one characteristic of $Fe^{2+}$ in a bare fourfold square planar coordination environment as it is observed for Fe(II)phtalocyanine as a reference. Instead, the spectra resemble those of air- or oxygen-exposed Fe(II)phtalocyanine [58, 59] and Fe–N–CNT materials [60] and thus may correspond to an intermediate-spin state $Fe^{2+}(I)$ present together with a $Fe^{3+}$ high-spin state. It should be noted that **A** and **B** had prolonged contact with air throughout. The branching ratios of the $L_3/L_2$ intensities indeed provide more details on the oxidation and spin state of iron [6, 60–63]. The $L_3/L_2$ ratios of an oxygen-exposed Fe(II)phtalocyanine have been calculated to be 3.76, corresponding to a combined contribution of a 30% $Fe^{2+}(I)$ intermediate spin ($Fe^{2+d}$) and 70% $Fe^{3+}$ high spin state [59]. In the present study, the $L_3/L_2$ ratio is 3.64 for **A** and 4.89 for **B**, the latter corresponding to a higher $Fe^{3+}$ contribution in **B** than in **A**.

**EXAFS** data have been studied for **A** under ambient conditions (air, room temperature). The Fe K-edge position is located at 7123 eV, corresponding to a $Fe^{3+}$ oxidation state, which is well above values for $Fe^0$ (7112 eV) and $Fe^{2+}$ (7117 eV). Experimental data were analyzed assuming a starting model with four nitrogen-bonding partners assumed to be located in the CNT tube structure and one axial single O atom coordinated to iron. Inclusion of other additional scattering paths such as additional Fe–Fe distances (characteristic for Fe–O–Fe oxide species) visibly increases the fit quality (Figures S10 and S11 and Table S2).

**$^{57}$Fe Mössbauer spectroscopy (MB)** has allowed the identification of iron-containing moieties like $FeN_4$, $FeN_{2+2}$, or $FeN_{4+1}$, $FeN_{4+2,}$ typically as doublets under ambient conditions [7]. Herein, MB spectra are recorded in the temperature range between 300 and 5 K with a $^{57}$Fe-enriched precursor solution of **1** for **A**, respectively, and the $^{57}$Fe-enriched ALD organometallic precursor **3** in the case of **B** due to the low active iron site concentration chosen (<<1%) for materials **A** and **B**. MB spectroscopy univocally confirms that neither of the aforementioned purely inorganic materials, namely, oxides, nitrides, and carbides, most often observed in synthetic pyrolysis approaches, are present in the Fe–N–C materials **A** and **B**. However, due to the aerobic conditions during sample handling, oxygen adsorption is very likely to occur on the embedded iron centers in **A** and **B**. It has been



26884062, 2026, 11, Downloaded from https://onlinelibrary.wiley.com/doi/10.1002/sstr.70646 by Karlsruher Institut Fur Technologie, Wiley Online Library on [19/11/2026]. See the Terms and Conditions (https://onlinelibrary.wiley.com/terms-and-conditions) on Wiley Online Library for rules of use; OA articles are governed by the applicable Creative Commons License

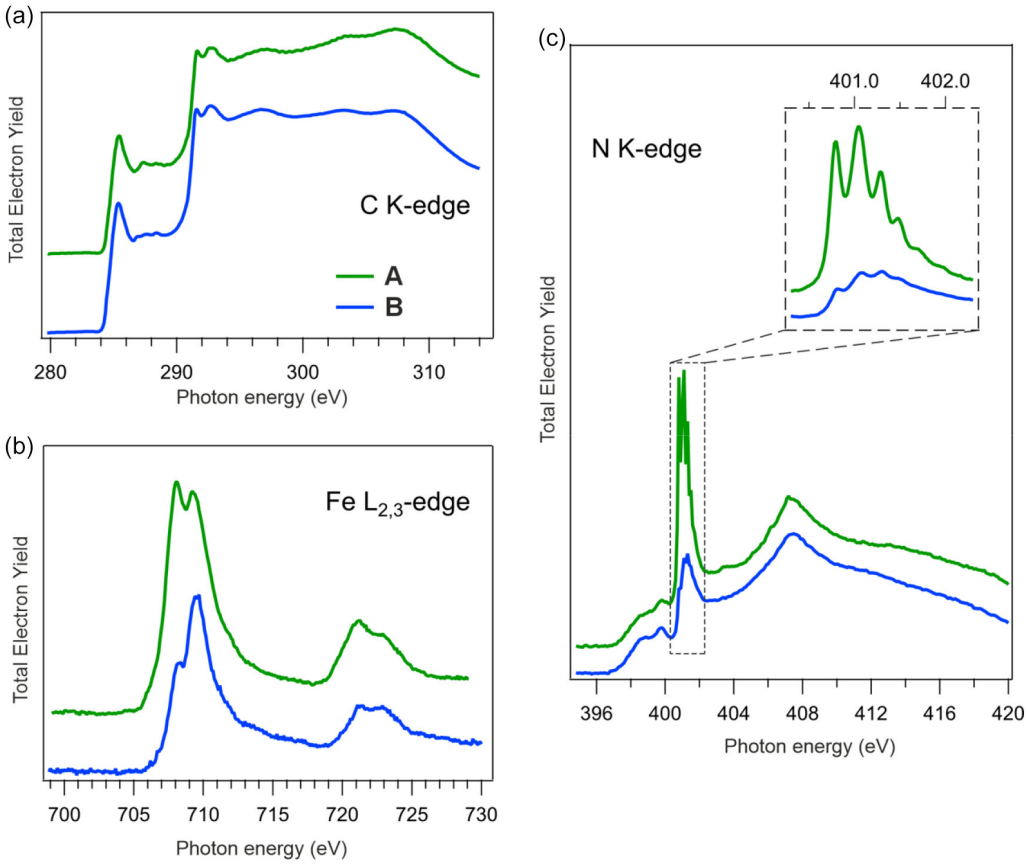



**FIGURE 4** | NEXAFS spectra (a) of the C K-edge and (b) Fe $L_{2,3}$-edge. Inset in (c) N K-edge shows the vibrational fine structure of molecular $N_2$ encased in the interior of the CNTs.

shown earlier, experimentally [64] and theoretically [65], that iron(II)phtalocyanine-containing $FeN_4$ entities are prone to partial oxidation or chemisorption of oxygen resulting in a $FeN_4O_2$ coordination. While oxygen is coordinated either in end-on or side-on mode, electron-acceptor surface states are formed. This gives rise to a significant electron transfer from $3d^6$ $Fe^{2+}$ (becoming $\delta^+$) toward the chemisorbed oxygen species (becoming $\delta^-$). The influence of oxygen adsorption results in a considerable narrowing of the HOMO/LUMO gap and the formation of a conduction band for the case of the $FeN_4$ framework upon oxysorption [65]. Here, we probe such an electronic scenario at Fe sites by $^{57}$Fe Mössbauer (MB) spectroscopy. In comparing the hyperfine parameters of **A** and **B** with MB parameters for the mostly observed doublets termed D1, D2, and D3 [66], we observe the presence of the so-called D1 site and absence of so-called D2,3 sites. The two latter are characterized by significantly larger quadrupole splittings (QS) and are typically assigned to square planar $Fe(II)N_4$ moieties without additional ligands [66–69]. The D1 site can be assigned to a Fe(III) high spin or a Fe(II) low spin state based on the center shift (CS) [21] in full accord with previous high-temperature pyrolysis-based approaches to Fe–N–C centers. Therein, quadrupole splittings between 0.7 and 1.0 mm $s^{-1}$ are attributed to ferrous low-spin or ferric high-spin $FeN_4$ moieties at which either $O_2$ or OH are adsorbed or coordinated [21–24].

The MB parameters for the second observed paramagnetic site, named D2$^{\#}$ herein (to be distinguishable from the reported D2 sites from the literature) in **A** and **B** (see Table S1), are in accord with $Fe^{2+}(I)$ intermediate spin sites in close agreement to our findings from NEXAFS studies.

Temperature-dependent MB spectra for **A** and **B** differ in the overall Fe concentration by about 30% (Figure 5). For the diluted case **B**, we fitted the spectra using the instrumental line width (Lorentzian, thin absorber limit). The line broadening for **A** affords a distribution model (xVBF) with significant Gaussian components of QS with $\sigma_{QS}$ of approx. ±0.25 mm/s (see shaded area in Figure 5 QS(T) right). Overall, QS and CS of the **A** site1 resemble a D1 Fe species; for further details, see Supporting Information [67]. The temperature dependence of the recoil-free fraction allows the discernment of the Lamb–Mössbauer parameters $\theta_{LM}$. $\theta_{LM}$ expresses the analog of the Debye–Waller factor, namely, the mean square isotropic thermal displacement $\langle x^2 \rangle$ of the Fe nuclei in the lattice. The Lamb–Mössbauer temperature can be interpreted as a macroscopic measure of the effective stiffness of the lattice. For **A**, we derived $\theta_{LM}$ of 155(10) K (**B** approx. 230(20) K) which is in line with the rapid decrease in spectral area upon heating. Such low $\theta_{LM}$ values are typically observed for other Fe–N–C materials [69]. However, CS (**A** site1 and 2) exhibit the same temperature dependence, which we fitted according to (Equation (1)) [70] to estimate the second-order Doppler shift (SOD) in order to obtain the Mössbauer-specific Debye temperature $\theta_M$. The SOD shift originates in a relativistic change in energy of the γ-photon due to thermal vibrations of the $^{57}$Fe nuclei and is proportional



26884062, 2026, 11, Downloaded from https://onlinelibrary.wiley.com/doi/10.1002/sstr.70646 by Karlsruher Institut Fur Technologie, Wiley Online Library on [19/11/2026]. See the Terms and Conditions (https://onlinelibrary.wiley.com/terms-and-conditions) on Wiley Online Library for rules of use; OA articles are governed by the applicable Creative Commons License

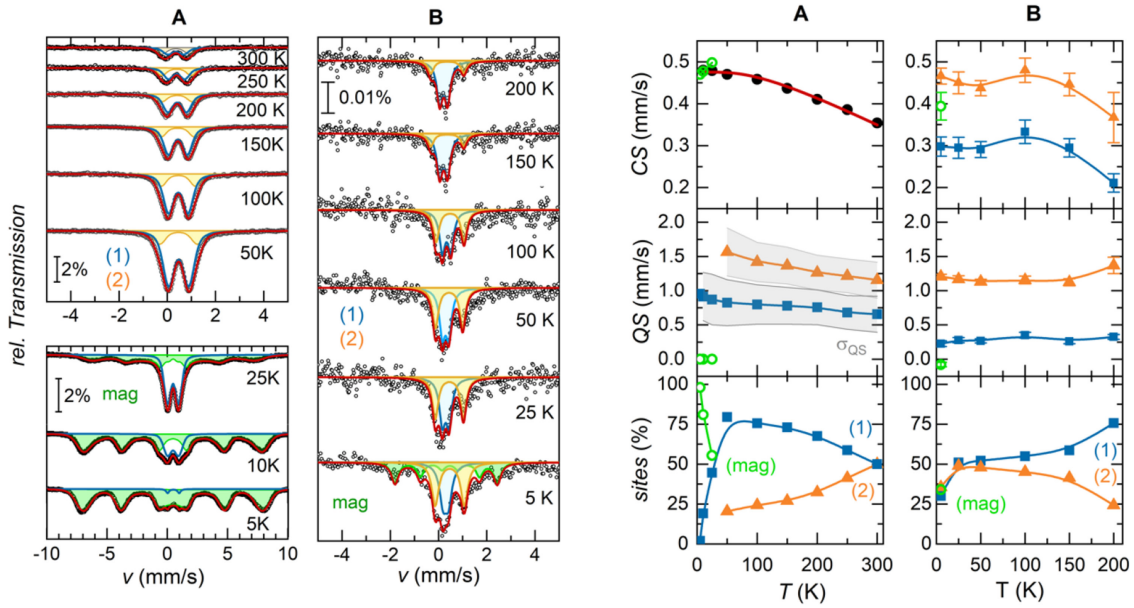



**FIGURE 5** | Left: $^{57}$Fe Mössbauer spectra of **A** and **B** in the temperature interval between 298 and 5 K. Right: Hyperfine parameters for **A** and **B**. The red line presents the fit to Equation (1). (For detailed MB data see Table S1.)

to the mean square velocity $\langle v^2 \rangle$ or the mean kinetic energy of the $^{57}$Fe nuclei.

$$\mathrm{CS}(T) = \mathrm{CS}_0 + \mathrm{CS}_{\mathrm{SOD}}(T) = \mathrm{CS}_0 - \frac{9k_{\mathrm{B}}E_\gamma}{16M_{\mathrm{eff}}c^2} \left(\theta_{\mathrm{M}} + 8T\left(\frac{T}{\theta_{\mathrm{M}}}\right)^3 \int_0^{\theta_{\mathrm{M}}/T} \frac{x^3}{e^x - 1}dx\right) \quad (1)$$

where $E_\gamma = 14.41$ keV is the energy of the Mössbauer transition, $M_{\mathrm{eff}}$ is the effective mass of the vibrating $^{57}$Fe nuclei (fixed to the isotopic mass of $^{57}$Fe, 53 095 MeV c$^{-2}$), $k_{\mathrm{B}}$ is the Boltzmann constant, and $c$ is the speed of light in vacuum.

We obtain $\theta_{\mathrm{M}} = 415(8)$ K for **A**, which corresponds to typical values of Fe in intermetallic phases. This suggests that overall, Fe is incorporated into the host and alters the charge carrier concentration of the conduction band and thereby adds to the conductivity of the materials. Interestingly, the slopes of CS (**B** site1 and 2) are rather similar to CS (**A**). The discrepancy of hyperfine parameters for site 1 and 2 in **B** is resolved and suggests that (i) the electric monopole interaction of the $^{57}$Fe nucleus with its surroundings and (ii) the electric field gradient EFG differ for **B** site1 and **B** site 2. The latter results in dissimilar QS values, which relate to a more isotropic environment (**B** site1) and increasing asymmetry for **B** site 2. Here, we treat site 2 as a second component of site 1, which may originate from an intermediate iron species $Fe^{2+\delta}$ within the observation time of the MB experiment (localization). One may speculate that for **A** with a higher Fe content, the dynamic charge localization for the **A** site 1 is the cause for the larger QS value with a significant $\sigma_{\mathrm{QS}}$ reflecting the distribution statistics of multiple sites. Concomitantly, the spectral area of **A** site 2 decreases relative to that of **A** site 1 toward lower temperatures.

At temperatures below 50 K, magnetic spectra are observed for **A**. These develop gradually and are composed of a distribution of hyperfine fields $H_{\mathrm{hf}}$. At 5 K, the majority of magnetic sites (66%) exhibit a $H_{\mathrm{hf}}$ (**A**) = 460(29) kOe, while the remaining fraction contributes via a broad distribution of smaller magnetic hyperfine fields. Sample **B** seems to develop magnetic fluctuations below 50 K as well (see change in CS values). However, these are still not sufficiently resolved at 25 K to be incorporated into the spectral fitting. At 5 K (Lorentzian line width increased by 20%), only a small magnetic fraction originating from both (**B** site 1 and 2) is observed. In this case, 35% almost static magnetic sites with $H_{\mathrm{hf}}$ (**B**) = 132 kOe are observed. Note that both paramagnetic sites (**B** site 1 and 2) remain present at 5 K.

## 2.5 | Magnetization Studies

In the following, we want to address the interplay of itinerant electrons with $^{57}$Fe centers embedded in the larger N-doped graphitic network of the highly conducting VA-NCNTs in **A** and **B**. The Ruderman–Kittel–Kasuya–Yoshida interaction (RKKY) [71, 72] describes the indirect exchange of localized magnetic moments via the polarization of conducting (delocalized) electrons. This exchange interaction is effective over large distances [73] and facilitates long-range magnetic coupling between spatially separated magnetic centers. Here, each iron site acts as a scattering center for conduction electrons, thereby polarizing the electronic states of the surrounding carbon network of the N-CNTs. To probe this scenario, we have performed magnetic measurements. Figure 6 depicts the $M(\mu_0 H)$ data for two different loaded samples **B**(ALD50) and **B**(ALD80) corrected for the significant diamagnetic contributions (**B**(ALD80): $-4.684 \times 10^{-6}$ emu/g and **B**(ALD50): $-2.860 \times 10^{-6}$ emu/g). Both materials exhibit approximately the expected saturation for $Fe^{3+}$ at 2 K and 8 T (see the Brillouin function). At 100 K, the magnetization is constant above 0.5 T, which corresponds to a Pauli paramagnetic contribution of a fully polarized metal. At applied magnetic fields below 0.5 T, hysteresis curves are observed. This suggests that dominant ferromagnetic correlations are present. The coercive fields are



26884062, 2026, 11, Downloaded from https://onlinelibrary.wiley.com/doi/10.1002/sstr.70646 by Karlsruher Institut Fur Technologie, Wiley Online Library on [19/11/2026]. See the Terms and Conditions (https://onlinelibrary.wiley.com/terms-and-conditions) on Wiley Online Library for rules of use; OA articles are governed by the applicable Creative Commons License

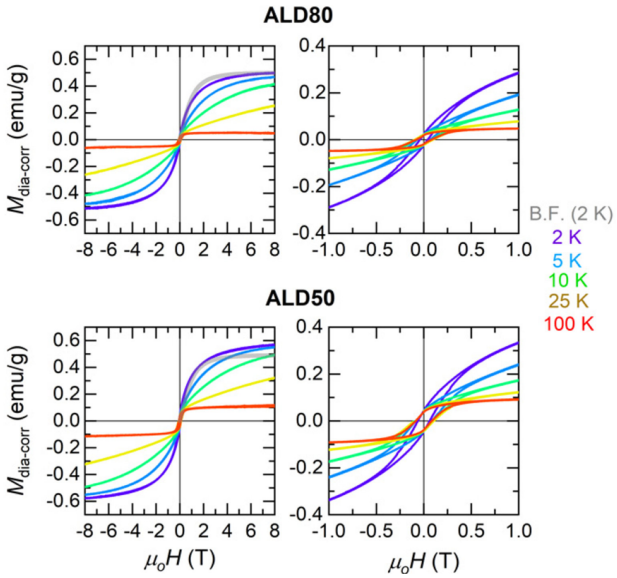



**FIGURE 6** | Magnetization data for **B**(ALD80) and **B**(ALD50) corrected for diamagnetic contribution. The Brillouin function (B.F.) at 2 K per Fe ($S = 2.5$, $g = 2.0$) is shown for comparison. Right panels are presenting the enlarged area of the hysteresis. (ALD50 and 80 denote number of deposition cycles leading to samples **B**.)

approximately 0.7 T, and the remanence is 0.02 emu/g (**B**(ALD80) and 0.04 emu/g **B**(ALD50) at 2 K, respectively.

## 2.6 | EPR Spectroscopy

To further examine the spin state of the embedded iron centers in **A** and **B**, CW X-band EPR spectra for nitrogen-free VACNTs and N-VACNTs are recorded at room temperature (Figure S12). For these iron-free samples, no pronounced paramagnetic resonance signals are observed under these conditions. Nevertheless, $Fe^{3+}$ centers in CNTs are often difficult to detect at X-band frequencies due to a combination of factors including low dopant concentration, strong line broadening caused by spin–spin interactions, or fast spin relaxation effects. In addition to that, the extended and typically well-graphitized network of CNTs acts as a strong microwave absorbing material, probing these extended $\pi$ structures to be difficult to stimulate. As a result, iron-related signals especially at low loadings of <<1% $Fe^{3+}$ may remain below the detection limit of X-band EPR. Therefore, X-band EPR spectra at room temperature showed no clear or pronounced resonance signals in iron-free or iron-loaded VA-NCNT samples. This indicates that most paramagnetic centers are either present in low concentration or are affected by fast spin relaxation, which broadens the signals and makes them difficult to detect under ambient conditions. To further resolve weak and overlapping contributions, high-field Q-band measurements were performed (Figure S13). In contrast to the X-band results, the Q-band spectra recorded at room temperature show a clear and sharp signal near $g \approx 2$, but only for the Fe-doped VA-NCNT sample. This signal is not observed in the undoped nitrogen-free VACNT for comparison. The narrow line width indicates that this signal originates from well-isolated paramagnetic centers with weak magnetic interactions. Its absence in the X-band suggests that it is masked there by the broad $g \approx 2$ background signal and limited spectral resolution. The sharp signal at $g \approx 2$ is most likely related to carbon-based radical centers that are enhanced or stabilized by the incorporated iron centers. The introduction of iron modifies the local carbon framework by creating additional defects and inducing charge transfer by forming Fe–O–C-type bonding configurations. Such effects can localize the spin density on carbon atoms in the CNT framework. In addition, exposure to oxygen leads to partial oxidation under ambient conditions introducing iron-oxo bonds as well as oxygen-containing functional groups such as hydroxyl or carbonyl species at defect sites or outer rim positions of the VA-NCNT framework stabilizing adjacent unpaired electrons. Structural defects such as vacancies, edge sites, and Stone–Wales-type defects can further contribute to the formation of localized radical states [74]. A minor contribution from isolated Fe-related centers cannot be excluded, but the sharp character of the signal suggests that carbon-centered radicals are the dominant origin. Upon lowering the temperature to 120 K, however, significant differences become visible as exemplified for solution-derived sample **A** (Figure 7). For **A**, distinct low-field resonances appear at $g_{eff} \approx 10.12$ and $g_{eff} \approx 6.16$, together with a very weak signal around $g_{eff} \approx 3.8$. These features are absent in the iron-free sample, confirming their origin from iron-related centers. The strong temperature dependence indicates that these centers are significantly influenced by spin relaxation effects. Fast relaxation occurring under ambient conditions suppresses these signals, while at 120 K, the relaxation slows down and the zero-field splitting becomes spectroscopically resolved.

These low-field resonances are characteristic of high-spin $Fe^{3+}$ ($S = 5/2$). The observed $g$-values are effective values arising from zero-field splitting rather than principal components of the $g$-tensor. The dominant signal at $g_{eff} \approx 6.16$ is typical for $Fe^{3+}$ in an axial or near-axial coordination environment. The additional feature at $g_{eff} \approx 10.12$ suggests an even more distorted component of the same spin system or the presence of a second $Fe^{3+}$ environment with different zero-field splitting parameters. The very weak signal at $g_{eff} \approx 3.8$ indicates that only a small fraction of $Fe^{3+}$ centers experiences significant rhombic distortion. These results show that iron is distributed over different local environments rather than occupying a single well-defined site [68]. In addition to the low-field

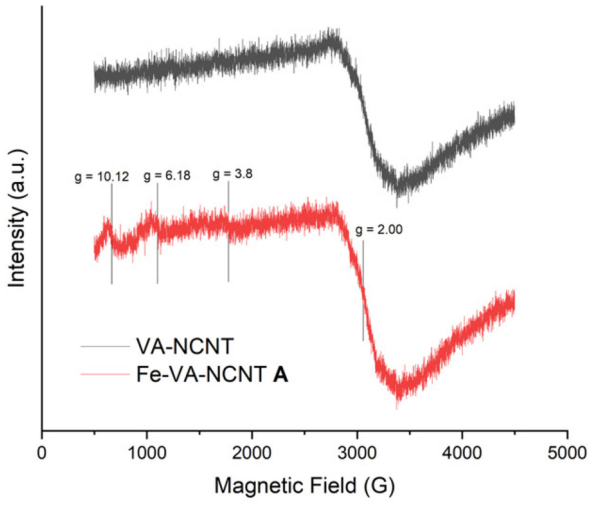



**FIGURE 7** | X-band EPR spectra of sample Fe@VACNT **A** together with iron free VA-NCNTs both measured at 120 K.



26884062, 2026, 11, Downloaded from https://onlinelibrary.wiley.com/doi/10.1002/sstr.70646 by Karlsruher Institut Fur Technologie, Wiley Online Library on [19/11/2026]. See the Terms and Conditions (https://onlinelibrary.wiley.com/terms-and-conditions) on Wiley Online Library for rules of use; OA articles are governed by the applicable Creative Commons License

Fe-related signals, both undoped and Fe-doped VA-NCNT samples exhibit a very broad signal around $g \approx 2$ at 120 K in the X-band. This signal has a Gaussian-like shape and is much broader than that of typical radical signals. Its presence in both samples of VA-NCNT and in **A** indicates that it originates from the CNT framework. It is attributed to a distribution of carbon-related paramagnetic states, including dangling-bond-like defects, disordered carbon regions, and localized π-electron states. The broad line width indicates an inhomogeneous broadening due to a wide distribution of local environments and weak spin–spin interactions. In the Fe-doped sample, an additional contribution from exchange-coupled Fe species or small Fe–O clusters may be present, but the dominant contribution is intrinsic to the carbon structure. It is important to note that the low-field $Fe^{3+}$ signals observed at 120 K in the X-band do not shift to $g \approx 2$ in the Q-band. The *g*-factor is frequency-independent, and the differences between the X-band and Q-band arise from the fact that different types of paramagnetic centers are detected with different sensitivity. The X-band at low temperature reveals zero-field-splitting-dominated $Fe^{3+}$ centers, whereas the Q-band at room temperature resolves weakly interacting and low-concentration species that are otherwise not visible. Overall, the combined EPR results show that Fe-doped VA-NCNTs in **A** and **B** contain several types of paramagnetic centers. The strong dependence on temperature and frequency highlights the importance of multifrequency EPR for understanding the complex defect structure in Fe-doped CNT systems.

## 2.7 | Positron Annihilation Studies (PALS)

For getting insight into the accessibility of possible catalytic Fe–N–C sites within the VA-NCNTs, PALS provide a sensitive tool for probing open-volume defects and porosity across multiple length scales, ranging from atomic vacancies to micro- and mesopores [75, 76]. PALS results in VA-NCNTs display three or four lifetime components, reflecting the presence of porosity and open-volume defects. The porosity-related lifetimes greater than 1 ns [77] correspond to *ortho*-positronium (o-Ps), while shorter lifetimes indicate annihilation in vacancies, vacancy clusters, and heteroatom-doped sites. In the current study, the latter are probably due to atomic doping of heteroatoms like nitrogen into the carbonaceous framework or to native defect sites in the tube walls. Focusing only on porosity-related o-Ps lifetimes, undoped VA-CNT and VA-NCNT feature three and two hierarchical micro- and mesopore groups, respectively (Figures 8 and S14). This hierarchical porosity allows access to atomically distributed catalytic sites as well as enabling transport of reactive gases throughout the interior of the CNT architecture. Mesoporosity arises from the narrow arrangement of tubes in the vertically arranged CNT architectures. During their synthesis, active species like $C_x$ fragments or neutral gases like $N_2$ are formed from the molecular precursors like pyridine [55, 56] and trapped inside the CNTs [57]. The main goal of utilizing positron annihilation was to examine the influence of N-doping in CNTs regarding their impact on defects and porosity.

In pristine nitrogen-free vertically aligned VACNTs, three pore families ($d_2$–$d_4$) are resolved, demonstrating a hierarchical porous network spanning 0.4–6.5 nm. For $E_p < 6$ keV (near-surface), $d_2$ remains nearly constant as the corresponding relative intensity $I_2$ increases, $d_3$ decreases with rising intensity, and both $d_4$ and $I_4$ decline, reflecting a transition from open surface voids toward more confined intertube spaces. At $E_p > 6$ keV (deeper regions), $d_2$ decreases alongside $I_2$, while $d_3$ and its intensity increase and $d_4$ holds steady in size with growing $I_4$, consistent with enhanced mesoporosity from interbundle voids, as corroborated by SEM/TEM imaging of the vertically aligned architecture. In the N-containing VACNT (VA-NCNT, pyridine-derived) sample, only two pore groups ($d_2$, $d_3$) are observed, indicating that nitrogen incorporation eliminates the largest void class ($d_4$) while preserving smaller pores amenable to Fe–$N_x$ site anchoring. Both $d_2$ and $d_3$ decrease up to ~6 keV and then stabilize, evidencing structural uniformity in the interior "bamboo-like" compartments seen in HRTEM/STEM–HAADF. Intensity $I_2$ remains low (~1.5%) and constant below 6 keV but reaches ~35% at higher energies, signaling a substantial intermediate-pore population at depth (likely in the walls of the columnar inter-tube channels for gas access). On the other hand, the negligible $I_3$ aligns with o-Ps quenching at pyridinic N and trapped $N_2$ sites. Overall, compared with pristine VA-CNTs, nitrogen incorporation refines the pore system by markedly suppressing both the number and maximum size of accessible mesopores over a large part of the implantation-energy range, thereby converting the initially strongly hierarchical, depth-graded pore system into a more uniform VA-NCNT architecture, with effective porosity predominantly located in the deeper regions.

## 2.8 | Oxygen Reduction Reaction (ORR)

Finally, Fe–N–C materials **A** and **B** have been investigated for catalytic activity in ORR in 0.1 M KOH, employing linear sweep

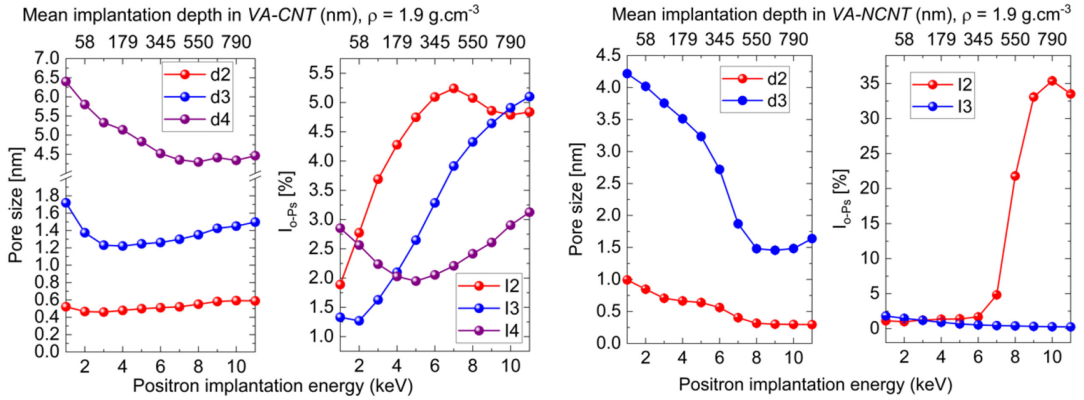



**FIGURE 8** | PALS showing the different life time components in VA-NCNTs in comparison to pristine nitrogen free VACNTs.



26884062, 2026, 11, Downloaded from https://onlinelibrary.wiley.com/doi/10.1002/sstr.70646 by Karlsruher Institut Fur Technologie, Wiley Online Library on [19/11/2026]. See the Terms and Conditions (https://onlinelibrary.wiley.com/terms-and-conditions) on Wiley Online Library for rules of use; OA articles are governed by the applicable Creative Commons License

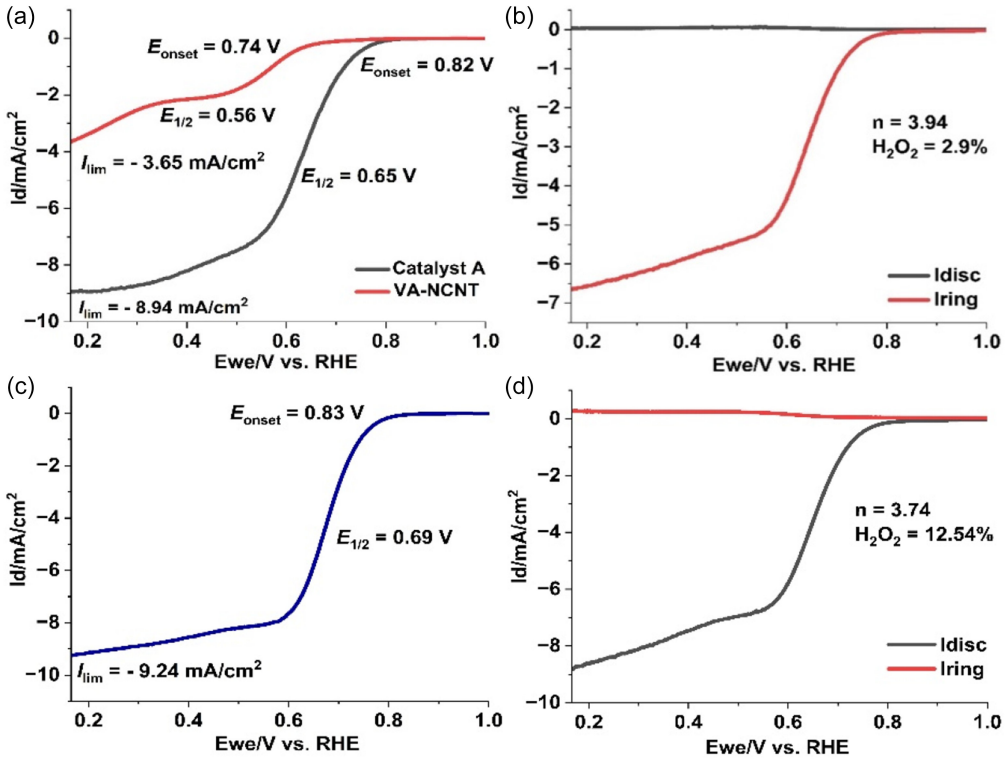



**FIGURE 9** | (a) Electrocatalytic activity of catalyst **A** in comparison to iron-free VA-NCNTs at 1600 rpm in RDE measurement. (b) RRDE curves of **A** at 1600 rpm showing 2.9% of $H_2O_2$ production. (c) The LSV curve of **B** at 1600 rpm. (d) RRDE curves of **B** at 1600 rpm showing 12.5% of $H_2O_2$ production.

voltammetry (LSV) (Figures 9, S15 and S16). Material **A** exhibits an effective activity with an onset potential ($E_{onset}$) of 0.82 V versus RHE and a half-wave potential ($E_{1/2}$) of 0.65 V versus RHE at 1600 rpm, indicating a significant improvement over native iron-free VA-NCNTs. The observed yield of $H_2O_2$ is below 3% as observed by RRDE (rotating ring-disc electrode) measurements, revealing that the electron transfer number is close to 4 ($n = 3.94$) and $H_2O_2$ formation is negligible. Values for $E_{onset}$ and $E_{1/2}$ for **A** are nearly comparable with CNT-based $FeN_5$ catalysts [42, 43]. Although the limiting current density for **A** ($I_{lim} = -8.94\,mA\,cm^{-2}$) is much higher than for the Pt/C catalyst and other CNT-based Fe–SACs [36–43], it is close and in agreement to the ORR activity of a VA-NCNT catalyst obtained by pyrolysis routes [25]. ALD-derived catalyst **B** shows a similar catalytic activity as **A**, with an onset potential ($E_{onset}$) of 0.83 V, a half-wave potential ($E_{1/2}$) of 0.69 V, and a limiting current density ($I_{lim}$) of $-9.24\,mA\,cm^{-2}$ at 1600 rpm (Figure 9). RRDE measurements, however, reveal a higher $H_2O_2$ (around 12%) formation. An electron-transfer number of $n = 3.74$ can thus be deduced (Figure 9d). It is noteworthy that the characteristics of the ORR activities of **A** and **B** are very similar bearing in mind their identical VA-NCNT host structure as well as comparable iron concentrations for both **A** and **B**.

## 3 | Conclusion

In our efforts to devise a more controlled alternative reaction pathway compared to the widely reported high-temperature pyrolytic approaches to Fe–N–C SAC catalysts, we focused on two unprecedented pyrolysis-free synthesis methods for Fe–SACs on VA-NCNTs. Both are synthetic techniques employing organometallic complexes either from solution or directly on the surface of the carbon support in an ALD-type approach and allow coordination of iron atoms under chimie-douce conditions into the N-CNT host. This allows to generate isolated catalytically active Fe–N–C centers. Both approaches are in stark contrast to high-temperature processes reported so far, which are unselective and often lead to a plethora of different inorganic products ranging from inorganic iron oxides, nitrides, and carbides to coordinatively embedded $FeN_x$ moieties. Both new synthetic routes are indeed atom-economic when introducing Fe single atoms in suitable surroundings, and they shed new light on formation pathways to such catalysts in the condensed phase. Fe–N–C catalysts **A** and **B** are, despite their low concentration in the N-VACNT framework, active in ORR. As proven by PALS, a significant amount of mesoporosity in the N-VACNT matrix is lost compared to a nitrogen-free VACNT structure. This could alter the mass transport throughout the dense VA-NCNT architecture and restrict the incorporation of Fe–N–C centers to the surface of the N-CNTs, making them probably slightly more accessible for further reactions and may explain their moderate ORR activity. XANES spectroscopy reveals iron in $Fe^{3+}$ and intermediate $Fe^{2+\delta}$($I$) spin states, indicating a coordination number >4 on iron due to an oxidative process of the iron centers located in the curved CNT walls. MB studies reveal the presence of a Fe(III) high spin species most obviously identical to the prominent D1 species in accord to elaborated experimental and theoretical studies of Fe–N–C sites in carbon matrices [67, 68]. This D1 Fe–N–C site may be present in the N-CNT surface layers and is most obviously in contact with adsorbed $O_2$ as a ligand. Therefore, iron(III) is most likely in a fivefold coordination geometry and still offers an additional accessible catalytic site, e.g., for the ORR. The observed magnetic behavior can be understood based on an indirect magnetic exchange



26884062, 2026, 11, Downloaded from https://onlinelibrary.wiley.com/doi/10.1002/sstr.70646 by Karlsruher Institut Fur Technologie, Wiley Online Library on [19/11/2026]. See the Terms and Conditions (https://onlinelibrary.wiley.com/terms-and-conditions) on Wiley Online Library for rules of use; OA articles are governed by the applicable Creative Commons License

between individual Fe–N–C sites through conduction electron of the N-CNT framework. This interaction is based on the RKKY mechanism between single iron centers, which are embedded in the conductive N-CNT surface.

## 4 | Experimental Section

### 4.1 | Synthesis of VA-NCNTs

VA-NCNTs were synthesized using the similar CVD process for VACNTs [78]. On a 2 cm × 2 cm $Si/SiO_2$ wafer, 40 nm $Al_2O_3$ was deposited by the ALD process, followed by a layer of 8 nm of Fe by plasma sputtering. The substrate along with the catalyst deposited was heated to the synthesis temperature of 925 °C in a reducing atmosphere with a gas flow of Ar (500 sccm) and $H_2$ (400 sccm). Once the set temperature was attained, synthesis was typically carried out for 30 min with pyridine as the carbon and nitrogen source. The synthesized VA-NCNTs were cooled under an argon atmosphere before being taken out at room temperature. The synthesized VA-NCNTs are multiwalled with a height of approx. 20–25 µm and a diameter of nearly 20 nm.

### 4.2 | Synthesis of Fe@NCNT Catalysts A and B

#### *4.2.1 | Synthesis of Bis($\eta^2$-ethylene)($\eta^6$-toluene)iron*

The solution of bis($\eta^2$-ethylene)($\eta^6$-toluene)iron precursor was prepared by following the reported method [28]. The metal-atom reactions took place in a 5-L custom-made, all-glass reactor (Figure 10) [79, 80]. The iron metal was evaporated using tungsten crucibles coated with aluminum oxide cement and calcined before use at temperatures above 600 °C under vacuum. During metal vaporization, approximately 20% of the metal is lost due to the unavoidable deposition of metal outside the reaction zone of metal atoms and toluene. Iron metal (500 mg, 8.77 mmol) was codeposited with toluene (130 mL) at −196 °C and $10^{-2}$ Pa over a period of 90 min. Then, the reaction vessel was filled with 25 L of ethylene gas and allowed to condense at −196 °C atop the codeposited solid toluene and iron metal. After warming up to −60 °C,

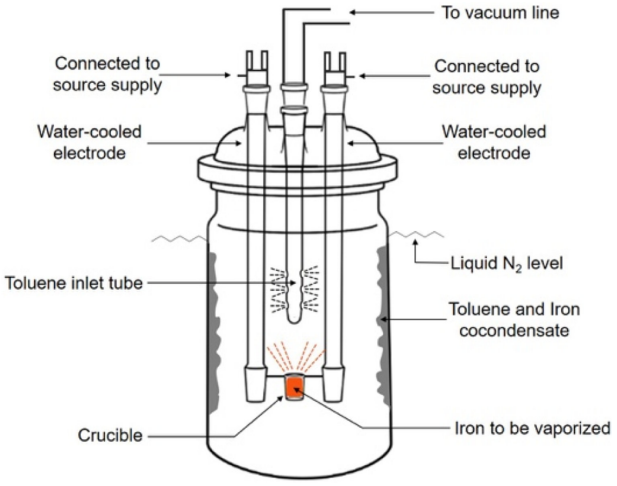



**FIGURE 10** | Schematics of the metal evaporation setup for co-condensation of Fe atoms and toluene and ethylene.

the melted suspension was stirred for 90 min at that temperature. Then, the unreacted metal was separated by filtration through a pad of aluminum oxide at −78 °C. The unreacted iron was treated with concentrated HCl to isolate 3.18 mmol of $FeCl_3 \cdot 6H_2O$. Considering both 20% loss and the amount of unreacted iron (with respect to the isolated amount of $FeCl_3 \cdot 6H_2O$), the concentration of iron in the solution was calculated to be 29.5 µmol/mL.

#### *4.2.2 | Reaction of Bis($\eta^2$-ethylene)($\eta^6$-toluene)iron With VA-NCNTs*

The VA-NCNTs along with substrate were placed in a Schlenk tube and kept under high vacuum for 30 min and flushed with argon gas three times to make sure that VA-NCNTs are completely free from air contamination. Then, the tube with VA-NCNTs was cooled to −30 °C by using a cooling bath. The solution of iron precursor (at −30 °C) was added slowly to the cooled VA-NCNTs containing Schlenk tube to submerge the sample completely in solution. Then, the cooling bath was removed, and the reaction tube was allowed to come to room temperature and kept for 24 h without any disturbance. After 24 h of reaction, the solution (Figure 10) was carefully transferred to another Schlenk tube, and the sample was washed three times with anhydrous toluene under argon. After washing, the sample was dried under vacuum to obtain catalyst **A**.

#### *4.2.3 | Synthesis of Bis(ethyl-cyclopentadienyl)iron $^{57}Fe(C_2H_5\text{-}Cp)_2$*

For the synthesis of $^{57}Fe(C_2H_5\text{-}Cp)_2$, a 100-mL Schlenk tube was charged with anhydrous $^{57}FeCl_2$ (1.15 g, 0.009 mol) and THF (25 mL) under argon. The resulting solution was cooled to −78 °C. A solution of Cp-$C_2H_5Na$ (2.2 g, 0.0188 mol) [80] in THF (30 mL) was prepared separately and added dropwise to the cooled $^{57}FeCl_2$ solution [81]. The final solution was stirred for 2 h at −78 °C and then stirred overnight at room temperature. The reaction mixture was further refluxed for 3 h and then filtered over Celite after cooling to room temperature. THF was removed by high vacuum, and the resulting dense solution was distilled under vacuum. $^{57}Fe(C_2H_5\text{–}Cp)_2$ (1.4 mL) was isolated as a yellow-orange liquid. For the synthesis of $^{57}Fe(C_2H_5\text{–}Cp)_2$, anhydrous $^{57}FeCl_2$ was obtained [82].

$^1$H NMR ($C_6D_6$, 300 MHz): $\delta$ 1.04–1.14 ppm (m, 6*H*, $CH_2$–$CH_3$), $\delta$ 2.13–2.30 ppm (m, 4*H*, $CH_2$–$CH_3$), $\delta$ 3.80–4.00 ppm (m, 8*H*, Cp). GC–MS: calc for $C_{14}H_{18}Fe$, 243.140; found 243.057.

#### *4.2.4 | ALD Synthesis of B*

The deposition of the Fe precursor over the VA-NCNTs was performed with an ALD Savannah S 100 system (Cambridge Ultratech) at a base pressure of 2.2 torr. During the process, the ALD reactor was set to a temperature of 250 °C, while a constant flow of carrier gas (argon) of 20 sccm was ensured. Prior to deposition, the VA-NCNT samples attached to the wafer were kept inside the ALD reactor for 20 min at 250 °C under a constant argon flow. The precursor $Fe(Cp\text{–}C_2H_5)_2$ was maintained at 60 °C. As a carrier gas, argon (99.9999%, AlphaGaz) was used and set to a constant flow of 20 sccm during the deposition process. The parameters for the single deposition cycle were as follows: pulse



26884062, 2026, 11, Downloaded from https://onlinelibrary.wiley.com/doi/10.1002/sstr.70646 by Karlsruher Institut Fur Technologie, Wiley Online Library on [19/11/2026]. See the Terms and Conditions (https://onlinelibrary.wiley.com/terms-and-conditions) on Wiley Online Library for rules of use; OA articles are governed by the applicable Creative Commons License

time Fe precursor: 1 s, pulse time $H_2$: 1 s, exposition time: 60 s, and wait time: 75 s. The most active single-atom catalyst **B** was generated after 50 ALD cycles.

### 4.3 | Materials Characterization

**Thermogravimetric analysis** was recorded on a Netzsch TG 209 F1 instrument under an ambient atmosphere.

**Raman spectroscopic studies** were carried out with a Thermo Scientific DXR3 Raman microscope.

**Transmission electron microscopy** was performed on a Philips XL30 FEG and a FEI Tecnai G2 F20 transmission electron microscope. HAADF–STEM characterization of **A** and **B** has been performed using a double-corrected TFS Themis Z TEM operated at 80 kV with a nominal beam current of 150 pA and probe diameter of 0.1 nm. The samples have been prepared by drop casting of the dispersed Fe@NCNTs in EtOH on a lacey carbon-coated Au TEM grid.

**Electron energy loss spectroscopy** (EELS) was performed using an Ametek (Gatan) GIF Continuum K3 HR spectrometer on Themis Z TEM. The EELS spectra were acquired in the STEM mode during repeated scanning of a sample area of around $100 \times 100\,nm^2$. The convergence angle of the electron probe is 30 mrad, and the collection angle is 40 mrad. The total integrated acquisition time is 297 s for the Fe L edge and 99 s for the N K edge. The presented core-loss edge was extracted from the raw spectrum after subtracting the background modeled by the power law.

**HRTEM** was performed with an FEI Tecnai G2 F20 with an operating voltage of 200 keV at FZ Jülich.

**$^{57}$Fe Mössbauer** spectra were collected in the transmission mode using a $^{57}$Co (Rh) source in a custom-built setup including a closed-cycle cryostat C2 (Montana Instruments). The temperature range was 5–300 K in a zero-applied field. All spectra were calibrated with respect to an α-Fe foil standard. All samples were dispersed in paraffin (40–42 °C m.p.). prior to the measurement. The Mössbauer spectra were analyzed using the Extended Voigt-based Fitting (xVBF) [83] method implemented in the Recoil software [84] to extract the Gaussian distribution of the quadrupole splittings and hyperfine magnetic fields for Fe sites. The half-width at half-maximum of the Lorentzian natural line was fixed to 0.147 mm/s.

**Magnetic measurements** were carried out in applied magnetic fields (+/−8T) at selected temperatures using the VSM option on a physical-property-measurement system (PPMS, Quantum Design). Sample masses were 1.5 mg (ALD80) and 1.8 mg (ALD50).

**XPS, NEXAFS, and EXAFS measurements** were carried out at the GELEM Dipole beamline at the BESSY II electron storage ring operated by the Helmholtz-Center Berlin for Materials and Energy [85]. Samples for the spectroscopic measurements were either prepared by gentle mechanical detachment from the silicon wafer or by rinsing the silicon wafer with ethanol and drying samples **A** and **B** under ambient conditions. The measurements were performed on the as-loaded samples. All measurements were performed at room temperature with a pressure in the analysis chamber of ca. $10^{-10}$ mbar. NEXAFS spectra were recorded in the total electron yield mode. XPS spectra were acquired with a Phoibos-150 electron energy analyzer. Photon energies for the single core levels were selected in a way to provide similar kinetic energies of emitted photoelectrons, i.e., similar probing depth. The photon energy was calibrated with the Au4f (Ebin_4f7/2 = 84.00) core level of the reference Au crystal. The fitting of XPS data was carried out with CasaXPS software.

X-ray absorption spectra (EXAFS) at the Fe K (7.112 keV) edge in fluorescence mode were collected at room temperature at the BAMline [86, 87] of the BESSY II synchrotron radiation facility operated by Helmholtz-Zentrum Berlin (HZB). X-rays from a 7 T wavelength shifter (WLS) were used. The X-ray beam was monochromatized with a Si(111) double-crystal monochromator, and intensities were measured using a custom-made 4-channel fluorescence detector. Each measurement was repeated min 5 times for more accurate statistics and then averaged. A thin Fe foil was used for energy calibration. Data processing, including edge calibration, background removal, and normalization, was performed with ATHENA software of the IFEFFIT package [88]. Measured spectra were summed, deglitched, corrected using pure metal foil, and smoothed (all spectra show relatively high noise due to their small thickness). Structure fitting of $x(R)$ functions obtained from the studied Fe K-edge EXAFS has been performed in the ARTEMIS software package with $k = 1$–$11$, $r = 1.25$–$4.00$, and single (Fe–N and Fe···C) and double scattering paths (N···C and N···N) with distances below 4 Å were used for fitting with fixed amplitude. For all distances, sigma$^2$ and dR were fitted independently. The Fe–O distance was also included in fitting.

**Positron annihilation spectroscopy (PALS)**: Variable-energy positron annihilation lifetime spectroscopy (VEPALS) measurements were performed on pristine VA-CNT and N-containing VA-NCNT samples at the mono-energetic positron source (MePS) beamline at HZDR, Germany [89]. Positron lifetime spectra were recorded using a digital lifetime detection system based on a $CeBr_3$ detector (51 mm diameter, 25.4 mm length) coupled to a Hamamatsu R13089-100 photomultiplier tube, shielded with μ-metal, and housed in a gold enclosure. Signal acquisition was carried out using a SPDevices ADQ14DC-2X digitizer with 14-bit vertical resolution and a sampling rate of $2\,GS\,s^{-1}$, yielding an overall time resolution of approximately 0.250 ns.

Each lifetime spectrum contained at least $1 \times 10^7$ counts to ensure reliable decomposition.

A typical lifetime spectrum, $N(t)$, the absolute value of the time derivative of the positron decay spectrum, is described by

$$N(t) = R(t) * \sum_{i=1}^{k+1} \frac{I_i}{\tau_i} e^{\frac{-t}{\tau_i}} + \text{background}$$

where $k$ is the number of different defect types contributing to the positron trapping, which are related to $k+1$ components in the spectra with the individual lifetimes $\tau_i$ and intensities $I_i$ ($\Sigma I_i = 1$) [90]. The instrument resolution function $R(t)$ is a sum of two Gaussian functions with distinct intensities and relative shifts both depending on the positron implantation energy, $E_p$. It



26884062, 2026, 11, Downloaded from https://onlinelibrary.wiley.com/doi/10.1002/sstr.70646 by Karlsruher Institut Fur Technologie, Wiley Online Library on [19/11/2026]. See the Terms and Conditions (https://onlinelibrary.wiley.com/terms-and-conditions) on Wiley Online Library for rules of use; OA articles are governed by the applicable Creative Commons License

was determined by the measurement and analysis of a reference sample, i.e., yttria-stabilized zirconia (YSZ), which exhibited a single well-known lifetime component. The background was negligible, hence fixed to zero. All the spectra were deconvoluted using a nonlinear least-squares fitting method, minimized by the Levenberg–Marquardt algorithm, employed within the fitting software package PALSfit [89] yielding three or four discrete lifetime components depending on the sample. The shortest lifetime component ($\tau_1$) is attributed to positron annihilation in small open-volume defects such as vacancy clusters within the CNT walls, while the longer lifetime components ($\tau_2$–$\tau_4$) correspond to positron or o-Ps annihilation in larger open and free volumes, including voids and micro- to mesoporous regions, respectively. The associated intensities ($I_1$–$I_4$) qualitatively reflect the relative abundance of these defect types, provided the compared open volumes are within a similar size regime.

In general, positron lifetime increases with increasing open- and free-volume size, as lower local electron densities reduce the annihilation probability and prolong the positron lifetime [91]. By varying the positron implantation energy $E_p$, depth-resolved information on defect sizes and their distribution throughout the CNT architecture is obtained, enabling a direct comparison of near-surface and bulk open-volume characteristics.

Variable-energy positron annihilation lifetime spectroscopy (VEPALS) measurements were performed on pristine VA-CNT and N-containing VA-NCNT samples at the mono-energetic positron source (MePS) beamline at HZDR, Germany [89]. Positron lifetime spectra were recorded using a digital lifetime detection system based on a $CrBr_3$ scintillator detector (51-mm diameter, 25.4-mm length) coupled to a Hamamatsu R13089-100 photomultiplier tube, shielded with μ-metal and housed in a gold enclosure. Signal acquisition was carried out using a SPDevices ADQ14DC-2X digitizer with 14-bit vertical resolution and a sampling rate of $2\,GS\,s^{-1}$, yielding an overall time resolution of approximately 0.205 ns.

The instrument resolution function employed for spectrum analysis was described by two Gaussian components with relative intensities and temporal shifts dependent on the positron implantation energy, $E_p$. Each lifetime spectrum contained at least $1 \times 10^7$ counts to ensure reliable decomposition. The measured lifetime distribution, $N(t)$, was analyzed according to the following:

$$N(t) = \Sigma\,(1/\tau_i)\,I_i \exp(-t/\tau_i)$$

where $\tau_i$ and $I_i$ denote the positron lifetime and relative intensity of the $i$-th component, respectively ($\Sigma I_i = 1$).

All spectra were deconvoluted using the nonlinear least-squares fitting software PALSfit [91], yielding three or four discrete lifetime components depending on the sample. The shortest lifetime component ($\tau_1$) is attributed to positron annihilation in small open-volume defects such as vacancy clusters within the CNT walls, while the longer lifetime components ($\tau_2$–$\tau_4$) correspond to annihilation in larger open volumes, including voids and micro- to mesoporous regions. The associated intensities ($I_1$–$I_4$) qualitatively reflect the relative abundance of these defect types, provided the compared open volumes are within a similar size regime.

In general, positron lifetime increases with increasing open-volume size, as lower local electron densities reduce the annihilation probability and prolong the positron lifetime [92]. By varying the positron implantation energy $E_p$, depth-resolved information on defect sizes and their distribution throughout the CNT architecture is obtained, enabling a direct comparison of near-surface and bulk open-volume characteristics.

To determine the Fe content in both catalysts, **ICP-OES analysis** was conducted in the SPECTRO GENESIS ICP-OES analyzer. The known amounts of Fe@VA-NCNT samples for **A** and **B** were digested separately in hot concentrated $HNO_3$ over a hot plate in a fume hood. After digestion, the solutions were cooled and filtered into volumetric flasks to remove the undigested solids. The volume of the solutions was adjusted with deionized water to reach the appropriate concentration for ICP-OES analysis.

**Electron paramagnetic resonance** (EPR) measurements were performed at room temperature using a dual-band Bruker E-500 ELEXSYS spectrometer. Measurements were performed both at room temperature and at 120 K. The spectrometer was mainly operated in the X-band mode at a microwave frequency of 9.88 GHz. In addition, Q-band (35 GHz) EPR measurements were carried out to achieve higher spectral resolution and improved sensitivity to $g$-value anisotropy. All spectra were recorded under identical experimental conditions to allow a reliable comparison between samples. Equal amounts of each sample were used in all measurements to ensure consistency and reproducibility. The microwave power was set to 0.5 mW, the magnetic-field modulation amplitude was 1 G, and the modulation frequency was 100 kHz. These parameters were carefully chosen to avoid signal saturation and distortion. All experimental settings were kept constant throughout the measurements.

**ORR measurements** were performed with a Bio-Logic potentiostat (Model VMP3) electrochemical workstation by implementing various techniques such as cyclic voltammetry (CV) and LSV. RDE and RRDE measurements were carried out over a BluRev RC-10K Rotating Disk (diameter of 3 mm) and Ring-Disk Electrode (diameter of disc 3 mm and for ring inner diameter = 4 mm and outer diameter = 6 mm). A three-electrode setup was assembled for the measurement: Catalyst mounted on glassy carbon disk (GC) as the working electrode, Pt rod as the counter electrode, and Hg/HgO as the reference electrode. For the preparation of catalyst slurry, 1.50 mg of the prepared sample, 250 μL of ethanol, and 15 μL of Nafion (5%) were mixed and ultrasonicated for 30 min. A 2.5 μL of catalyst slurry was drop cast on the surface of the GC disk of RDE (or RRDE) and dried at room temperature to be used as a working electrode with a catalyst loading of $0.2\,mg/cm^2$. The ORR test was performed in $O_2$-saturated 0.1 M KOH by sweeping the potential from 0.3 to −0.7 V at a scan rate of 10 mV/s with electrode rotation at 400, 600, 900, 1600, and 2500 rpm, and $O_2$ gas was purged continuously into the solution at a flow rate of 25 sccm through an 8-mm fritted tube (Lenz Laborglas GmbH & Co). For the RRDE tests, the disk electrode was scanned at a rate of 10 mV/s, and the ring potential was held at 0.3 V (vs. Hg/HgO). The following equations were used to calculate the percentage of peroxide species in relation to total oxygen reduction products and the number of electrons involved during the ORR process:

$$HO_2^- = 200\frac{I_r/N}{I_d + I_r/N}$$



26884062, 2026, 11, Downloaded from https://onlinelibrary.wiley.com/doi/10.1002/sstr.70646 by Karlsruher Institut Fur Technologie, Wiley Online Library on [19/11/2026]. See the Terms and Conditions (https://onlinelibrary.wiley.com/terms-and-conditions) on Wiley Online Library for rules of use; OA articles are governed by the applicable Creative Commons License

$$n = 4\frac{I_d}{I_d + I_r/N}$$

here, $I_d$ and $I_r$ are the disk and ring currents, respectively, and $N$ is the current collection efficiency of the Pt ring ($N = 0.46$) from the reduction of $K_3Fe(CN)_6$ [93]. The potential values versus Hg/HgO have been converted to the potential values versus RHE by following the literature [94].


## Acknowledgments

We thank Ildiko Balog, Sudher Kumar Yadav, and Sandeep Yadav (all at TUDa) for the synthesis of the iron ALD precursors (IB), initial advice and guidance in electrochemical measurements (SKY), and introduction to the VA-NCNT synthesis (SY). J.E. is grateful to the ERC at FZ Jülich for the possibility to measure HRTEM under a long-term cooperation contract of TUDa with ERC. HZDR scientists (MOL, AGA, MB, AW) are grateful to the facility staff of HZDR, Dresden-Rossendorf, for technical support. This work was funded by the Deutsche Forschungsgemeinschaft (DFG) subprojects B06 and A04 within the first funding period of the CRC 1487 "Iron, upgraded!"

Open Access funding enabled and organized by Projekt DEAL.

## Funding

This study was supported by Deutsche Forschungsgemeinschaft.


## Conflicts of Interest

The authors declare no conflicts of interest.

## Data Availability Statement

The data that support the findings of this study are available in the Supporting Information of this article.

## References


1. H. Fei, Z. Dong, Y. Feng, et al., "General Synthesis and Definitive Structural Identification of $MN_4C_4$ Single-Atom Catalysts with Tunable Electrocatalytic Activities," *Nature Catalysis* 1 (2018): 63–72, https://doi.org/10.1038/s41929-017-0008-y.

2. Z. Yang, Y. Wang, M. Zhu, et al., "Boosting Oxygen Reduction Catalysis with Fe–$N_4$ Sites Decorated Porous Carbons toward Fuel Cells," *ACS Catalysis* 9 (2019): 2158–2163, https://doi.org/10.1021/acscatal.8b04381.

3. C.-X. Zhao, B.-Q. Li, J.-N. Liu, and Q. Zhang, "Intrinsische Elektrokatalytische Aktivitätssteuerung Von M-N-C-Einzelatom-Katalysatoren für Die Sauerstoffreduktionsreaktion," *Angewandte Chemie* 133 (2021): 4496–4512, https://doi.org/10.1002/ange.202003917.

4. A. Zitolo, V. Goellner, V. Armel, et al., "Identification of Catalytic Sites for Oxygen Reduction in Iron- and Nitrogen-Doped Graphene Materials," *Nature Materials* 14 (2015): 937–942, https://doi.org/10.1038/nmat4367.

5. M. Chen, Y. He, J. S. Spendelow, and G. Wu, "Atomically Dispersed Metal Catalysts for Oxygen Reduction," *ACS Energy Letters* 4 (2019): 1619–1633, https://doi.org/10.1021/acsenergylett.9b00804.

6. M. Xiao, J. Zhu, L. Ma, et al., "Microporous Framework Induced Synthesis of Single-Atom Dispersed Fe-N-C Acidic ORR Catalyst and Its In Situ Reduced Fe-$N^4$ Active Site Identification Revealed by X-Ray Absorption Spectroscopy," *ACS Catalysis* 8 (2018): 2824–2832, https://doi.org/10.1021/acscatal.8b00138.

7. U. I. Kramm, L. Ni, and S. Wagner, "$^{57}$Fe Mössbauer Spectroscopy Characterization of Electrocatalysts," *Advanced Materials* 31 (2019): 1805623, https://doi.org/10.1002/adma.201805623.

8. N. Segura-Salas, V. Gridin, V. A. Saveleva, et al., "Influence of the Purification Strategy on the Activity and Stability of FeNC Catalysts for the Oxygen Reduction Reaction," *Journal of Physical Chemistry C* 129 (2025): 18439–18450, https://doi.org/10.1021/acs.jpcc.5c04548.

9. N. Ohri, Y. Hua, R. Baidoun, and D. Kim, "Pyrolytic Synthesis of Carbon-Supported Single-Atom Catalysts," *Chem Catalysis* 3 (2023): 100837, https://doi.org/10.1016/j.checat.2023.100837.

10. X. Ao, W. Zhang, Z. Li, et al., "Unraveling the High-Activity Nature of Fe–N–C Electrocatalysts for the Oxygen Reduction Reaction: The Extraordinary Synergy between Fe–$N_4$ and $Fe_4N$," *Journal of Materials Chemistry A* 7 (2019): 11792–11801, https://doi.org/10.1039/C9TA02338K.

11. J. A. Varnell, E. C. M. Tse, C. E. Schulz, et al., "Identification of Carbon-Encapsulated Iron Nanoparticles as Active Species in Non-Precious Metal Oxygen Reduction Catalysts," *Nature Communications* 7 (2016): 12582, https://doi.org/10.1038/ncomms12582.

12. R. Li, X. Li, Q. Liu, H. Yue, Y. Meng, and Y. Tian, "Effect of Fe–N–C Single Atom/Cluster Catalyst on ORR of PEMFC," *International Journal of Hydrogen Energy* 139 (2025): 718–729, https://doi.org/10.1016/j.ijhydene.2025.05.294.

13. R. Zeng, Y. Yang, X. Feng, et al., "Nonprecious Transition Metal Nitrides as Efficient Oxygen Reduction Electrocatalysts for Alkaline Fuel Cells," *Science Advances* 8 (2022): eabj1584, https://doi.org/10.1126/sciadv.abj1584.

14. D. Mladenović, A. Mladenović, D. M. F. Santos, et al., "Transition Metal Oxides for Bifunctional ORR/OER Electrocatalysis in Unitized Regenerative Fuel Cells," *Journal of Electroanalytical Chemistry* 946 (2023): 117709, https://doi.org/10.1016/j.jelechem.2023.117709.

15. K. Strickland, E. Miner, Q. Jia, et al., "Highly Active Oxygen Reduction Non-Platinum Group Metal Electrocatalyst without Direct Metal–Nitrogen Coordination," *Nature Communications* 6 (2015): 7343, https://doi.org/10.1038/ncomms8343.

16. T. Al-Zoubi, W. Gao, C. E. Schulz, et al., "Effects of Superparamagnetic Iron Nanoparticles on Electrocatalysts for the Reduction of Oxygen," *Inorganic Chemistry* 60 (2021): 4236–4242, https://doi.org/10.1021/acs.inorgchem.0c03298.

17. T. Asset and P. Atanassov, "Iron-Nitrogen-Carbon Catalysts for Proton Exchange Membrane Fuel Cells," *Joule* 4 (2020): 33–44, https://doi.org/10.1016/j.joule.2019.12.002.

18. C. Gallenkamp, Y.-J. Song, N. von Rhein, G. L. Motis, R. Valentí, and V. Krewald, "Electronic Complexity of Active Site Models for FeNC Catalysts: A Systematic Study of Truncation Effects in Molecular and Periodic Models," *The Journal of Physical Chemistry C* 129 (2025): 17407–17419, https://doi.org/10.1021/acs.jpcc.5c02746.

19. L. Ni, C. Gallenkamp, S. Paul, et al., "Active Site Identification in FeNC Catalysts and TheirAssignment to the Oxygen Reduction Reaction Pathway by In Situ $^{57}$Fe Mössbauer Spectroscopy," *Advanced Energy and Sustainability Research* 2 (2021): 2000064, https://doi.org/10.1002/aesr.202000064.

20. L. Ni, C. Gallenkamp, S. Wagner, E. Bill, V. Krewald, and U. I. Kramm, "Identification of the Catalytically Dominant Iron Environment in Iron- and Nitrogen-Doped Carbon Catalysts for the Oxygen Reduction Reaction," *Journal of the American Chemical Society* 144 (2022): 16827–16840, https://doi.org/10.1021/jacs.2c04865.

21. C. Gallenkamp, U. I. Kramm, J. Proppe, and V. Krewald, "Calibration of Computational Mössbauer Spectroscopy to Unravel Active Sites in FeNC Catalysts for the Oxygen Reduction Reaction," *International Journal of Quantum Chemistry* 121 (2021): e26394, https://doi.org/10.1002/qua.26394.





26884062, 2026, 11, Downloaded from https://onlinelibrary.wiley.com/doi/10.1002/sstr.70646 by Karlsruher Institut Fur Technologie, Wiley Online Library on [19/11/2026]. See the Terms and Conditions (https://onlinelibrary.wiley.com/terms-and-conditions) on Wiley Online Library for rules of use; OA articles are governed by the applicable Creative Commons License

22. J. Li, S. Ghoshal, W. Liang, et al., "Structural and Mechanistic Basis for the High Activity of Fe–N–C Catalysts toward Oxygen Reduction," *Energy & Environmental Science* 9 (2016): 2418–2432, https://doi.org/10.1039/C6EE01160H.

23. D. Menga, J. L. Low, Y.-S. Li, et al., "Resolving the Dilemma of Fe–N–C Catalysts by the Selective Synthesis of Tetrapyrrolic Active Sites via an Imprinting Strategy," *Journal of the American Chemical Society* 143 (2021): 18010–18019, https://doi.org/10.1021/jacs.1c04884.

24. D. Menga, F. E. Wagner, and T.-P. Fellinger, "Life Cycle of Single Atom Catalysts: A Mössbauer Study on Degradation and Reactivation of Tetrapyrrolic Fe–N–C Powders," *Materials Horizons* 10 (2023): 5577–5583, https://doi.org/10.1039/D3MH00308F.

25. J. S. Bates, J. J. Martinez, M. N. Hall, et al., "Chemical Kinetic Method for Active-Site Quantification in Fe-N-C Catalysts and Correlation with Molecular Probe and Spectroscopic Site-Counting Methods," *Journal of the American Chemical Society* 145 (2023): 26222–26237, https://doi.org/10.1021/jacs.3c08790.

26. J. L. Low, C. Roth, and B. Paulus, "Exploring the Inner- and Outer-Sphere Mechanistic Pathways of ORR on M–N–Cs with Pyrrolic $MN_4$ Motifs," *The Journal of Physical Chemistry C* 128 (2024): 5075–5083, https://doi.org/10.1021/acs.jpcc.4c00299.

27. M. Ferrandon, A. J. Kropf, D. J. Myers, et al., "Multitechnique Characterization of a Polyaniline–Iron–Carbon Oxygen Reduction Catalyst," *The Journal of Physical Chemistry C* 116 (2012): 16001–16013, https://doi.org/10.1021/jp302396g.

28. U. Zenneck and W. Frank, "Bis($\eta^2$-Ethene)($\eta^6$-Toluene)iron," *Angewandte Chemie International Edition* 25 (1986): 831–833, https://doi.org/10.1002/anie.198608311.

29. N. Chakrapani, B. Wei, A. Carrillo, P. M. Ajayan, and R. S. Kane, "Capillarity-Driven Assembly of Two-Dimensional Cellular Carbon Nanotube Foams," *Proceedings of the National Academy of Sciences* 101 (2004): 4009–4012, https://doi.org/10.1073/pnas.0400734101.

30. Z. Liang, N. Kong, C. Yang, et al., "Highly Curved Nanostructure-Coated Co, N-Doped Carbon Materials for Oxygen Electrocatalysis," *Angewandte Chemie International Edition* 60 (2021): 12759–12764, https://doi.org/10.1002/anie.202101562.

31. J. Yang, Z. Wang, C.-X. Huang, et al., "Compressive Strain Modulation of Single Iron Sites on Helical Carbon Support Boosts Electrocatalytic Oxygen Reduction," *Angewandte Chemie International Edition* 60 (2021): 22722–22728, https://doi.org/10.1002/anie.202109058.

32. Y. Zhu, Y. Jiang, H. J. W. Li, et al., "Tip-Like Fe–$N_4$ Sites Induced Surface Microenvironments Regulation Boosts the Oxygen Reduction Reaction," *Angewandte Chemie International Edition* 63 (2024): e202319370, https://doi.org/10.1002/anie.202319370.

33. G. Chen, R. Lu, C. Li, et al., "Hierarchically Porous Carbons with Highly Curved Surfaces for Hosting Single Metal $FeN_4$ Sites as Outstanding Oxygen Reduction Catalysts," *Advanced Materials* 35 (2023): 2300907, https://doi.org/10.1002/adma.202300907.

34. L. Yang, D. Cheng, H. Xu, et al., "Unveiling the High-Activity Origin of Single-Atom Iron Catalysts for Oxygen Reduction Reaction," *Proceedings of the National Academy of Sciences* 115 (2018): 6626–6631, https://doi.org/10.1073/pnas.1800771115.

35. K. J. Klabunde, *Nanocatalysis*, (Academic Press, 1994), ISBN: 0-12-410760-S.

36. Y. Xia, K. D. Gilroy, H.-C. Peng, and X. Xia, "Seed-Mediated Growth of Colloidal Metal Nanocrystals," *Angewandte Chemie International Edition* 56 (2017): 60–95, https://doi:10.1002/anie.201604731.

37. N. T. K. Thanh, N. Maclean, and S. Mahiddine, "Mechanisms of Nucleation and Growth of Nanoparticles in Solution," *Chemical Reviews* 114 (2014): 7610–7630, https://doi.org/10.1021/cr400544s.

38. M. Sleutel, J. Lutsko, A. E. S. Van Driessche, M. A. Durán-Olivencia, and D. Maes, "Observing Classical Nucleation Theory at Work by Monitoring Phase Transitions with Molecular Precision," *Nature Communications* 5 (2014): 5598, https://doi.org/10.1038/ncomms6598.

39. K. Gong, F. Du, Z. Xia, M. Durstock, and L. Dai, "Nitrogen-Doped Carbon Nanotube Arrays with High Electrocatalytic Activity for Oxygen Reduction," *Science* 323 (2009): 760–764, https://doi.org/10.1126/science.1168049.

40. D. Guo, R. Shibuya, C. Akiba, S. Saji, T. Kondo, and J. Nakamura, "Active Sites of Nitrogen-Doped Carbon Materials for Oxygen Reduction Reaction Clarified Using Model Catalysts," *Science* 351 (2016): 361–365, https://doi.org/10.1126/science.aad0832.

41. Y. Imizu and K. J. Klabunde, "Solvated Metal Atom Dispersed Catalysts," in *Catalysis of Organic Reactions*, 1st ed. ed. R. L. Augustine (CRC Press, 1985).

42. L. Lai, J. R. Potts, D. Zhan, et al., "Exploration of the Active Center Structure of Nitrogen-Doped Graphene-Based Catalysts for Oxygen Reduction Reaction," *Energy & Environmental Science* 5 (2012): 7936–7942, https://doi.org/10.1039/C2EE21802J.

43. J. Zhang, Z. Xia, and L. Dai, "Carbon-Based Electrocatalysts for Advanced Energy Conversion and Storage," *Science Advances* 1 (2015): e1500564, https://doi.org/10.1126/sciadv.1500564.

44. P. Cui, L. Zhao, Y. Long, L. Dai, and C. Hu, "Carbon-Based Electrocatalysts for Acidic Oxygen Reduction Reaction," *Angewandte Chemie International Edition* 62 (2023): e202218269, https://doi.org/10.1002/anie.202218269.

45. K. Hayashida, J. Nakamura, and K. Takeyasu, "Why Does the Performance of Nitrogen-Doped Carbon Electrocatalysts Decrease in Acidic Conditions," *Angewandte Chemie International Edition* 64 (2025): e202502702, https://doi.org/10.1002/anie.202502702.

46. S. Sarkar, S. Niyogi, E. Bekyarova, and R. C. Haddon, "Organometallic Chemistry of Extended Periodic π-Electron Systems: Hexahapto-Chromium Complexes of Graphene and Single-Walled Carbon Nanotubes," *Chemical Science* 2 (2011): 1326–1333, https://doi.org/10.1039/C0SC00634C.

47. F. Wang, M. E. Itkis, E. Bekyarova, S. Sarkar, X. Tian, and R. C. Haddon, "Solid-State Bis-Hexahapto-Metal Complexation of Single-Walled Carbon Nanotubes," *Journal of Physical Organic Chemistry* 25 (2012): 607–610, https://doi.org/10.1002/poc.1959.

48. X. Tian, S. Sarkar, M. L. Moser, et al., "Effect of Group 6 Transition Metal Coordination on the Conductivity of Graphite Nanoplatelets," *Materials Letters* 80 (2012): 171–174, https://doi.org/10.1016/j.matlet.2012.04.086.

49. E. Bekyarova, S. Sarkar, F. Wang, et al., "Effect of Covalent Chemistry on the Electronic Structure and Properties of Carbon Nanotubes and Graphene," *Accounts of Chemical Research* 46 (2013): 65–76, https://doi.org/10.1021/ar300177q.

50. I. P. Gloriozov, R. Marchal, J.-Y. Saillard, and Y. F. Oprunenko, "Chromium Tricarbonyl and Chromium Benzene Complexes of Graphene, Their Properties, Stabilities, and Inter-Ring Haptotropic Rearrangements – A DFT Investigation," *European Journal of Inorganic Chemistry* 2015 (2015): 250–257, https://doi.org/10.1002/ejic.201402879.

51. Y. Cheng, S. Zhao, B. Johannessen, et al., "Atomically Dispersed Transition Metals on Carbon Nanotubes with Ultrahigh Loading for Selective Electrochemical Carbon Dioxide Reduction," *Advanced Materials* 30 (2018): 1706287, https://doi.org/10.1002/adma.201706287.

52. H. C. Choi, S. Y. Bae, J. Park, et al., "Experimental and Theoretical Studies on the Structure of N-Doped Carbon Nanotubes: Possibility of Intercalated Molecular $N_2$," *Applied Physics Letters* 85 (2004): 5742–5744, https://doi.org/10.1063/1.1835994.

53. Z. Li, L. Zhang, D. E. Resasco, B. S. Mun, and F. G. Requejo, "Angle-Resolved X-Ray Absorption Near Edge Structure Study of Vertically Aligned Single-Walled Carbon Nanotubes," *Applied Physics Letters* 90 (2007): 103115, https://doi.org/10.1063/1.2709506.



26884062, 2026, 11, Downloaded from https://onlinelibrary.wiley.com/doi/10.1002/sstr.70646 by Karlsruher Institut Fur Technologie, Wiley Online Library on [19/11/2026]. See the Terms and Conditions (https://onlinelibrary.wiley.com/terms-and-conditions) on Wiley Online Library for rules of use; OA articles are governed by the applicable Creative Commons License

54. L. G. Bulusheva, E. O. Fedorovskaya, A. G. Kurenya, and A. V. Okotrub, "Supercapacitor Performance of Nitrogen-Doped Carbon Nanotube Arrays," *Physica Status Solidi B* 250 (2013): 2586–2591, https://doi.org/10.1002/pssb.201300108.

55. M. Terrones, R. Kamalakaran, T. Seeger, and M. Rühle, "Novel Nanoscale Gas Containers: Encapsulation of $N_2$ in $CN_x$ Nanotubes," *Chemical Communications* 36 (2000): 2335–2336, https://doi.org/10.1039/B008253H.

56. A. V. Okotrub, L. G. Bulusheva, A. G. Kudashov, V. V. Belavin, D. V. Vyalikh, and S. L. Molodtsov, "Orientation Ordering of $N_2$ Molecules in Vertically Aligned $CN_x$ Nanotubes," *Applied Physics A* 94 (2009): 437–443, https://doi.org/10.1007/s00339-008-4914-3.

57. C. Kramberger, T. Thurakitseree, H. Koh, et al., "One-Dimensional $N_2$ Gas Inside Single-Walled Carbon Nanotubes," *Carbon* 55 (2013): 196–201, https://doi.org/10.1016/j.carbon.2012.12.026.

58. P. L. Cook, X. Liu, W. Yang, and F. J. Himpsel, "X-Ray Absorption Spectroscopy of Biomimetic Dye Molecules for Solar Cells," *The Journal of Chemical Physics* 131 (2009): 194701, https://doi.org/10.1063/1.3257621.

59. P. S. Miedema, M. M. van Schooneveld, R. Bogerd, et al., "Oxygen Binding to Cobalt and Iron Phthalocyanines as Determined from In Situ X-Ray Absorption Spectroscopy," *The Journal of Physical Chemistry C* 115 (2011): 25422–25428, https://doi.org/10.1021/jp209295f.

60. J. Zhou, P. N. Duchesne, Y. Hu, et al., "Fe–N Bonding in a Carbon Nanotube–Graphene Complex for Oxygen Reduction: An XAS Study," *Physical Chemistry Chemical Physics* 16 (2014): 15787–15791, https://doi.org/10.1039/C4CP01455C.

61. F. M. F. de Groot, "X-Ray Absorption and Dichroism of Transition Metals and Their Compounds," *Journal of Electron Spectroscopy and Related Phenomena* 67 (1994): 529–622, https://doi.org/10.1016/0368-2048(93)02041-J.

62. F. de Groot, "Multiplet Effects in X-Ray Spectroscopy," *Coordination Chemistry Reviews* 249 (2005): 31-63, https://doi.org/10.1016/j.ccr.2004.03.018.

63. P. A. van Aken and B. Liebscher, "Quantification of Ferrous/Ferric Ratios in Minerals: New Evaluation Schemes of Fe L 23 Electron Energy-Loss Near-Edge Spectra," *Physics and Chemistry of Minerals* 29 (2002): 188–200, https://doi.org/10.1007/s00269-001-0222-6.

64. S. C. Dahlberg and M. E. Musser, "Electron Acceptor Surface States due to Oxygen Adsorption on Metal Phthalocyanine Films," *The Journal of Chemical Physics* 72 (1980): 6706–6711, https://doi.org/10.1063/1.439130.

65. B. Białek and P. Bragiel, "Influence of Oxygen Adsorption on Electronic Structure of Iron Phthalocyanine," *Acta Physica Polonica A* 89 (1996): 443–449.

66. S. Farida and J.-H. Wang, "Iron-Involved ORR Electrocatalysts under the Lens of In-Situ/Operando Mössbauer Spectroscopy," *Journal of Electrochemistry* 32 (2026): 2506261, https://doi.org/10.61558/2993-074X.3578.

67. T. Mineva, I. Matanovic, P. Atanassov, et al., "Understanding Active Sites in Pyrolyzed Fe–N–C Catalysts for Fuel Cell Cathodes by Bridging Density Functional Theory Calculations and $^{57}$Fe Mössbauer Spectroscopy," *ACS Catalysis* 9 (2019): 9359–9371, https://doi.org/10.1021/acscatal.9b02586.

68. K. Abdiaziz, L. Ni, D. Demirbas, et al., "Reversibly Redox-Active Iron Oxide Structures in FeNC Catalysts Identified by Microscopy and Spectroelectrochemical EPR and Mössbauer Methods," *Journal of the American Chemical Society* 148 (2026): 3995–4007, https://doi.org/10.1021/jacs.5c12396.

69. M. T. Sougrati, V. Goellner, A. K. Schuppert, L. Stievano, and F. Jaouen, "Probing Active Sites in Iron-Based Catalysts for Oxygen Electro-Reduction: A Temperature-Dependent $^{57}$Fe Mössbauer Spectroscopy Study," *Catalysis Today* 262 (2016): 110–120, https://doi.org/10.1016/j.cattod.2015.10.017.

70. P. Gütlich, E. Bill, and A. X. Trautwein, Mössbauer Spectroscopy and Transition Metal Chemistry: Fundamentals and Applications (Springer-Verlag, 2011), https://doi.org/10.1007/978-3-540-88428-6.

71. J. N. Lalena, Principles of Inorganic Materials Design, 3rd ed., (Wiley, 2020), 387, ISBN: 978-1-119-48676-3.

72. J. H. Van Vleck, "Note on the Interactions between the Spins of Magnetic Ions or Nuclei in Metals," *Reviews of Modern Physics* 34 (1962): 681–686, https://doi.org/10.1103/RevModPhys.34.681.

73. J. Girovsky, J. Nowakowski, M. E. Ali, et al., "Long-Range Ferrimagnetic Order in a Two-Dimensional Supramolecular Kondo Lattice," *Nature Communications* 8 (2017): 15388, https://doi.org/10.1038/ncomms15388.

74. T. Feng, X. Ruan, Z. Ye, and B. Cao, "Spectral Phonon Mean-Free Path and Thermal Conductivity Accumulation in Defected Graphene: The Effects of Defect Type and Concentration," *Physical Review B* 91 (2015): 224301, https://doi.org/10.1103/PhysRevB.91.224301.

75. K. Ito and Y. Kobayashi, "Variable-Energy Positron Annihilation as Highly Sensitive Nanoporosimetry for Porous Thin Films," *Acta Physica Polonica A* 107 (2005): 717–723.

76. A. G. Attallah, V. Bon, K. Maity, et al., "Revisiting Metal–Organic Frameworks Porosimetry by Positron Annihilation: Metal Ion States and Positronium Parameters," *The Journal of Physical Chemistry Letters* 15 (2024): 4560–4567, https://doi.org/10.1021/acs.jpclett.4c00762.

77. I. Mincov, M. P. Petkov, P. Tsou, and T. Troev, "Porosity Characterization of Aerogels Using Positron Annihilation Lifetime Spectroscopy," *Journal of Non-Crystalline Solids* 350 (2004): 253–258, https://doi.org/10.1016/j.jnoncrysol.2004.06.024.

78. D. J. Babu, M. Bruns, and J. J. Schneider, "Unprecedented $CO_2$ Uptake in Vertically Aligned Carbon Nanotubes," *Carbon* 125 (2017): 327–335, https://doi.org/10.1016/j.carbon.2017.09.047.

79. K. J. Klabunde, P. L. Timms, P. S. Skell, and S. Ittel, "Introduction to Metal Atom Syntheses," *Inorganic Syntheses* 19 (1979): 59–70, https://doi.org/10.1002/9780470132500.ch11.

80. K. J. Klabunde and Y. Tanaka, "The Building of a Catalytic Metal Particle One Atom at a Time: Solvated Metal Atom Dispersed Catalysts," *Journal of Molecular Catalysis* 21 (1983): 57–79, https://doi.org/10.1016/0304-5102(93)80111-7.

81. A. N. Nesmeyanov, K. N. Anisimov, and Z. P. Valueva, "Preparation of (ethylcyclopentadienyl) Manganese Tricarbonyl," *Bulletin of the Academy of Sciences of the USSR Division of Chemical Science* 10 (1961): 1659–1661.

82. M. Aresta, C. F. Nobile, and D. Petruzzelli, "Iron(0) Oxidation by Hydrogen Chloride in Tetrahydrofuran: A Simple Way to Anhydrous Iron(II) Chloride," *Inorganic Chemistry* 16 (1977): 1817–1818, https://doi.org/10.1021/ic50173a050.

83. K. Lagarec and D. G. Rancourt, "Extended Voigt-Based Analytic Lineshape Method for Determining N-Dimensional Correlated Hyperfine Parameter Distributions in Mössbauer Spectroscopy," *Nuclear Instruments and Methods in Physics Research Section B* 129 (1997): 266–280, https://doi.org/10.1016/S0168-583X(97)00284-X.

84. K. Lagarec and D. G. Rancourt, Recoil – Mössbauer Spectral Analysis Software for Windows, (Department of Physics, University of Ottawa, 1998).

85. S. I. Fedoseenko, D. V. Vyalikh, I. E. Iossifov, et al., "Commissioning Results and Performance of the High-Resolution Russian–German Beamline at BESSY II," *Nuclear Instruments and Methods in Physics Research Section A* 505 (2003): 718–728, https://doi.org/10.1016/S0168-9002(03)00624-7.

86. H. Riesemeier, K. Ecker, W. Görner, B. R. Müller, M. Radtke, and M. Krumrey, "Layout and First XRF Applications of the BAMline at BESSY II," *X-Ray Spectrometry* 34, no. 2 (2005): 160–163.



26884062, 2026, 11, Downloaded from https://onlinelibrary.wiley.com/doi/10.1002/sstr.70646 by Karlsruher Institut Fur Technologie, Wiley Online Library on [19/11/2026]. See the Terms and Conditions (https://onlinelibrary.wiley.com/terms-and-conditions) on Wiley Online Library for rules of use; OA articles are governed by the applicable Creative Commons License

87. A. G. Buzanich, M. Radtke, K. V. Yusenko, et al., "BAMline, A Real-Life Sample Materials Research Beamline," *The Journal of Chemical Physics* 158, no. 24 (2023): 244202.

88. B. Ravel and M. Newville, "ATHENA, ARTEMIS, HEPHAESTUS: Data Analysis for X-Ray Absorption Spectroscopy Using IFEFFIT," *Journal of Synchrotron Radiation* 12, no. 4 (2005): 537–541.

89. A. Wagner, M. Butterling, M. O. Liedke, K. Potzger, and R. Krause-Rehberg, "Positron Annihilation Lifetime and Doppler Broadening Spectroscopy at the ELBE Facility," *AIP Conference Proceedings* 1970 (2018): 040003, https://doi.org/10.1063/1.5040215.

90. R. Krause-Rehberg and H. S. Leipner, "Positron Annihilation in Semiconductors," in Solid-State Sciences, (Springer-Verlag, 1999).

91. J. V. Olsen, P. Kirkegaard, N. J. Pedersen, and M. Eldrup, "PALSfit: A New Program for the Evaluation of Positron Lifetime Spectra," *Physica Status Solidi C* 4 (2007): 4004–4006, https://doi.org/10.1002/pssc.200675868.

92. F. Tuomisto and I. Makkonen, "Defect Identification in Semiconductors with Positron Annihilation: Experiment and Theory," *Reviews of Modern Physics* 85 (2013): 1583–1631, https://doi.org/10.1103/RevModPhys.85.1583.

93. T. N. Kumar, S. Sivabalan, N. Chandrasekaran, and K. L. Phani, "Synergism between Polyurethane and Polydopamine in the Synthesis of Ni–Fe Alloy Monoliths," *Chemical Communications* 51 (2015): 1922–1925, https://doi.org/10.1039/C4CC07534J.

94. K. Kawashima, R. A. Márquez, Y. J. Son, et al., "Accurate Potentials of Hg/HgO Electrodes: Practical Parameters for Reporting Alkaline Water Electrolysis Overpotentials," *ACS Catalysis* 13 (2023): 1893–1898, https://doi.org/10.1021/acscatal.2c05655.

## Supporting Information

Additional supporting information can be found online in the Supporting Information section.



26884062, 2026, 11, Downloaded from https://onlinelibrary.wiley.com/doi/10.1002/sstr.70646 by Karlsruher Institut Fur Technologie, Wiley Online Library on [19/11/2026]. See the Terms and Conditions (https://onlinelibrary.wiley.com/terms-and-conditions) on Wiley Online Library for rules of use; OA articles are governed by the applicable Creative Commons License